

1 **Zircon perspectives on the age and origin of evolved S-type granites from the Cornubian Batholith,**  
2 **southwest England**

3 \*W.D. Smith<sup>1,2</sup>, J.R. Darling<sup>2</sup>, D.S. Bullen<sup>2</sup>, S. Lasalle<sup>2</sup>, I. Pereira<sup>2</sup>, H. Moreira<sup>2</sup>, C.J. Allen<sup>2</sup> & S. Tapster<sup>3</sup>

4 <sup>1</sup>School of Earth & Ocean Sciences, Cardiff University, United Kingdom

5 <sup>2</sup>School of Earth & Environmental Sciences, University of Portsmouth, United Kingdom

6 <sup>3</sup>NERC Isotope Geoscience Laboratories, British Geological Survey, Keyworth, United Kingdom

7 \*Corresponding Author: [smithwd1@cardiff.ac.uk](mailto:smithwd1@cardiff.ac.uk)

8 **Abstract**

9 Granite stocks across southwest England have played a significant role in the genesis of world-class  
10 polymetallic mineralisation. This study presents the first geochemical and geochronological dataset  
11 for the composite Crownhill stock, placing it into the newly emerging geochronological framework for  
12 the Cornubian Batholith. The Crownhill stock comprises kaolinised two-mica granite in the north and  
13 variably-grained biotite granite in the south that encloses pods of tourmaline granite. All granites are  
14 peraluminous ( $A/CNK > 1$ ) and the biotite (BG) and tourmaline granites (TG) are related by the  
15 replacement of biotite by tourmaline and secondary muscovitization. Integrated LA-ICP-MS and CA-  
16 ID-TIMS geochronology indicate two-phase magmatism, where zircon cores yield  $288.9 \pm 5$  Ma and  
17  $286.4 \pm 5$  Ma and rims yield  $277.74 \pm 0.33$  Ma and  $278.35 \pm 0.35$  Ma, for BG and TG respectively. The  
18 zircon cores crystallised during initial magmatism, that formed the two-mica and muscovite granites  
19 (e.g., Carnmenellis, Bodmin, and Hemerdon) exposed in the north of the Crownhill stock. The zircon  
20 rims crystallised from the second phase of magmatism the formed the biotite and tourmaline granites  
21 (e.g., Dartmoor and St. Austell). This indicates that zircon crystals were assimilated from older two-  
22 mica and muscovite granites and entrained in the second phase of magmatism. Trace element  
23 compositions of zircon grains suggest that the rims crystallised from a more evolved magma, where  
24 zircon grains hosted in tourmaline granites are broadly more evolved than those from biotite granites.

25 This is likely a result of elevated volatile concentrations delaying zircon fractionation. Trace cassiterite  
26 has been observed within interstitial tourmaline in the tourmaline granites, where crystallisation was  
27 likely induced by the removal of boron through tourmaline fractionation, coupled with the addition of  
28 Sn sourced from the alteration of biotite. The assimilation and over-printing of older granites by  
29 second-stage magmatism suggests that the initial phase of magmatism could be more widespread  
30 than initially thought and that tourmalinisation may have been responsible for leaching and  
31 remobilising Sn from the biotite-rich granites.

32 **Keywords:** S-type granite, zircon, U-Pb geochronology, geochemistry, tin-tungsten, Cornubian  
33 Batholith

34

## 35 1. Introduction

36 Peraluminous granites [ $Al_2O_3 > (Na_2O + K_2O + CaO)$ ] occur in orogens across the world (e.g., Sylvester,  
37 1998; Yang et al., 2016), often hosting world-class magmatic and magmatic-hydrothermal ore  
38 deposits (Černý et al., 2005; Romer & Kroner, 2016). The Variscan granites of the Cornubian Batholith  
39 (Figure 1) were emplaced during early Permian post-collisional extension (Shail & Wilkinson, 1994;  
40 Shail & Leveridge, 2009; Simons et al., 2016). Their diachronous emplacement has governed the  
41 distribution of tin-tungsten (Sn-W) mineralisation (Jackson et al., 1989; Chesley et al., 1993; Simons et  
42 al., 2017). However, recent literature highlights a decoupling between major W- and Sn-forming  
43 events, controlled by differing degrees of partial melting of a metasedimentary protolith (Simons et  
44 al., 2017). The granites close temporal relationship has made delineating discrete phases of  
45 magmatism problematic, augmented by the effects of secondary alteration.

46 Zircon U-Pb geochronological studies focussed on the crystallisation of the Cornubian  
47 Batholith have been largely avoided since S-type granites typically retain a large proportion of  
48 inherited zircon grains (Chesley et al., 1993; Neace et al., 2016). In addition, zircon grains hosted in

49 evolved granites typically contain high U ( $\gg 100$  ppm) concentrations and can therefore, rapidly  
50 become metamict (Romer et al., 2007). Thus, the long-standing chronological framework for the  
51 granites and associated mineralisation of the region has relied on Rb-Sr whole-rock isochrons  
52 (Darbyshire & Shepherd, 1985, 1987) and U-Th-Pb monazite or xenotime studies (Chesley et al., 1993;  
53 Chen et al., 1993; Clark et al., 1993). However, the Rb-Sr method is susceptible to resetting during low  
54 grade metamorphism (Evans, 1989) and the monazite U-Pb system can be partially reset below 900°C,  
55 facilitated by fluid-rock interaction (Williams et al., 2011). New studies have shown that carefully  
56 selected magmatic zircon grains are more reliable geochronometers for peraluminous granite  
57 emplacement than previously anticipated (Alvarado et al., 2013; Laurent et al., 2017) allowing for new  
58 U-Pb and trace element studies to better understand the temporal relationships between granite  
59 types and their associated processes.

60           Some of the least understood granites are located in the eastern Cornubian Batholith. This  
61 region encompasses the Dartmoor pluton, which incorporates Lee Moor to the south, adjacent to the  
62 Crownhill and Hemerdon stocks, the latter representing a world-class tungsten deposit (Figure 1).  
63 These granites were previously believed to be the southern extremity of the Dartmoor pluton (Beer &  
64 Scrivener, 1982). Ar-Ar muscovite dating has indicated that the metalliferous Hemerdon granite has a  
65 minimum emplacement age of  $290 \pm 0.4$  Ma (Chesley et al. 1993) and therefore, over 10 Myr older  
66 than Dartmoor (Figure 2). This study presents the first U-Pb ages and trace element compositions of  
67 zircon crystals in the Crownhill stock. We aim to refine the petrogenetic model for the granites  
68 exposed in the region, whilst examining the implications that granite magmatism has on Sn-W  
69 mineralisation.

## 70 **2. Regional Setting**

71 Southwest England is primarily composed of Devonian and Carboniferous successions, deposited in an  
72 short-lived marginal or successor basin to the Rheic Ocean (e.g., Franke, 2000; Shail & Leveridge,  
73 2009). Rifting in the Early Devonian prompted the formation of a transient passive margin, within

74 which sedimentary successions and rift-related basaltic magmas were emplaced (e.g., Leveridge &  
75 Hartley, 2006). The Variscan convergence between Gondwana, Laurussia, and subordinate peri-  
76 Gondwana micro-plates was initiated in the Late Devonian (e.g., Shail & Leveridge, 2009; Kroner &  
77 Romer, 2013), where continental collision in the Early Carboniferous triggered thin-skinned  
78 deformation and regional epizonal-anchizonal metamorphism (Isaac et al., 1982; Warr et al., 1991).  
79 During the Early Permian, convergence was succeeded by regional dextral transtension, which  
80 reactivated early-Variscan thrusts and associated transfer faults (Shail & Wilkinson, 1994; Shail &  
81 Alexander, 1997). The NNE-SSW lithospheric extension led to the emplacement of post-collisional  
82 granites and coeval mafic intrusives (Shail & Alexander, 1997; Dupius et al., 2015), alongside  
83 contemporaneous aplites and rhyolites ('elvans') that locally intrude granites (Simons et al., 2016).

84         The Cornubian Batholith extends from the Isle of Scilly to Dartmoor and comprises six major  
85 plutons and numerous smaller granitic stocks (Figure 1; Dangerfield & Hawkes, 1981). Bott et al.  
86 (1958) suggested that the exposed granite plutons are cupolas of a single composite batholith that  
87 extends for approximately 250x40 km (Taylor, 2007). However, more recent geochronological  
88 investigations (e.g., Chesley et al., 1993; Chen et al., 1993; Tapster et al., 2017) reveal that granite  
89 emplacement was progressive over approximately 25 million years.

90         The batholith displays considerably textural and mineralogical variation (e.g., Dangerfield &  
91 Hawkes, 1981; Simons et al., 2016; Figure 1). A crustal origin for the granites has been proposed (e.g.,  
92 Exley & Stone 1982; Jackson et al., 1989; Chappell & Hine, 2006; Simons et al., 2016, 2017), where a  
93 feldspathic metagreywacke is suggested as the protolith (Chappell & Hine, 2006; Simons et al., 2016).  
94 The oldest granites (300-288 Ma) represent two-mica (e.g., Bodmin and Carnmenellis) and muscovite  
95 granites (e.g., Hemerdon and Carn Brea; Figure 2), whereas the younger granites (284-274 Ma) are  
96 composed of composite biotite and tourmaline granites (e.g., Dartmoor, St. Austell and Land's End).  
97 Simons et al. (2016) propose a two-stage emplacement model, where the older granites formed  
98 through muscovite dehydration melting (731-806°C, >5 kbar), induced by magmatic underplating

99 during ongoing convergence. Increasing temperatures and declining pressures in the lower crust  
100 resulted in the melting of more refractory minerals and biotite (770-850°C, 4 kbar), producing the  
101 later biotite-dominated granites, which fractionated to produce tourmaline granites. Smaller  
102 tourmaline granite pods or orbicules occur in association with biotite granites, likely formed through  
103 tourmalinisation (Alderton et al., 1980).

104 The Crownhill stock is composed of a megacrystic biotite-rich core, bound by a variably-  
105 grained biotite granite to the south and a kaolinised two-mica granite to the north (Knox & Jackson,  
106 1990; Figure 1). This is the only stock that comprises granites deriving from both inferred phases of  
107 magmatism. Pods of tourmaline granite occur in the biotitic granites of Crownhill and Lee Moor. The  
108 advanced weathering of the stock negates a significant geochemical study to resolve its petrogenesis,  
109 however, accessory phase geochronology and geochemistry could provide evidence for two-phase  
110 magmatism and help elucidate the petrogenetic relationship between the two.

### 111 3. Sampling & Analytical Methods

112 The granites at Crownhill and Lee Moor (Lee Moor pit) are variably kaolinised, and sampling targeted  
113 the least weathered outcrops for geochemical and geochronological analysis. An additional biotite  
114 granite sample was collected Blackenstone Quarry in northeast Dartmoor (Figure 1). Polished thin  
115 sections were produced at the University of Portsmouth (UoP) for petrological analysis and samples  
116 were crushed using standard jaw-crushing and disc-mill techniques. A subsample was powdered for  
117 geochemical analysis by XRF, and the remainder was sieved to extract the 50-355 µm fraction from  
118 which zircon grains were separated using standard density and magnetic methods at UoP and the  
119 University of Bristol. Approximately 200 zircon grains were hand-picked, mounted in epoxy resin, and  
120 polished to half-height. Zircon grains were imaged via secondary and backscattered electron  
121 techniques to identify compositional domains and mineral defects using a Zeiss EVO MA10 LaB6  
122 scanning electron microscope at UoP. Inclusions were identified using energy dispersive spectroscopy  
123 (Oxford Instruments with Aztec Software). Cathodoluminescence (CL) imaging was attempted, but a

124 very low CL response was detected from these grains, which is attributed to their relatively high U  
125 contents (MacRae et al., 2014).

126 The powdered sample for XRF analysis was mixed at a 10:1 ratio with a lithium-  
127 metatetraborate flux to produce a homogeneous fusion bead for major element analysis. Pressed  
128 powder pellets were used for trace element analysis. A WD Rigaku Primus II XRF was used for  
129 measuring major and trace elements and was quantitatively analysed against matrix-matched  
130 standards from USGS (JG-1a, JG-3 and JR1). Elements were measured within 5% of their reference  
131 values, where MgO and TiO<sub>2</sub> measured within 20% for JR-1 and JG-3, respectively. Additional trace  
132 elements (including REEs) were measured in fragments of the fusion beads by laser ablation  
133 inductively-coupled plasma mass spectrometry (LA-ICP-MS) using a New Wave UP-213 Nd-YAG 213  
134 nm ablation system, coupled to an Agilent 7500cs Q-ICP-MS. Over two analytical sessions, the  
135 machines were optimized using NIST-612 and analyses were standardized to JR1, JG-1a, JG3 and NIST-  
136 614 were run as secondary standards to monitor accuracy and precision (Imai et al., 1995). Elements  
137 fall within 10% of their published values, whereas Zn, La, EU, Tb, Hf and Ta fall within 20%. Data were  
138 reduced using SILLS (Guillong et al., 2008; see Electronic Appendix 1 and 2).

139 U-Pb geochronological analysis of zircon was conducted using an ASI RESolution Excimer 193  
140 nm excimer ablation system, coupled to an Analytik Jena Plasma Quant MS, followed by the approach  
141 detailed by Moreira et al. (2018). Zircon grains were ablated using 10-15 µm spots (4.5 Jcm<sup>2</sup>, 2 Hz)  
142 over four analytical sessions. NIST-612 was used to optimise each analytical session, where acceptable  
143 tuning criteria included <0.2% oxide production (ThO<sup>+</sup>/Th<sup>+</sup> and UO<sup>+</sup>/U<sup>+</sup>) and <sup>232</sup>Th/<sup>238</sup>U=1. Plešovice  
144 was used as the primary standard to correct for instrumental mass bias, using the reference values in  
145 Sláma et al. (2008). Temora 2 (Black et al., 2004), BB9 (Santos et al., 2017) and GJ-1 (Jackson et al.,  
146 2004) were analysed as secondary standards, all of which within error of their published values (see  
147 Electronic Appendix 3). Monazite U-Th-Pb geochronology used the same instrumentation and were  
148 ablated using 5 µm diameter spots (2 Jcm<sup>2</sup>, 1`Hz). Results were calibrated against primary standard

149 Itambé over one analytical session (Gonçalves et al., 2016), and FC-1 was analysed as a secondary  
150 standard (Horstwood et al., 2003).

151 All intercept ages in Tera-Wasserburg regressions are anchored to a  $^{207}\text{Pb}/^{206}\text{Pb}$  value of 0.85  
152 ( $\pm 0.05$ ) after the Stacey & Kramers (1975) model. Data were reduced in Iolite 3.4 and laser-induced  
153 elemental fractionation was corrected using an exponential regression. No common Pb correction  
154 was applied (see Electronic Appendix 3).

155 Concordant zircon grains utilised for LA-ICP-MS were removed from the epoxy mounts and  
156 fragmented to remove the tips from the zircon grains, ahead of chemical abrasion isotope dilution  
157 thermal ionization mass spectrometry (CA-ID-TIMS). Zircon tips are used instead of whole zircon to  
158 bias results towards emplacement ages and not inherited or antecrystic ages. The chemical abrasion  
159 process was based on that of Mattinson (2005) varying leaching times between 8-12 hours based on  
160 the size of the zircon fragment analysed. Ion exchange chemistry and subsequent isotopic analysis  
161 were carried out at NIGL, British Geological Survey using the ET535 tracer, with isotopic ratios  
162 measured using a Thermo-Triton thermal ionisation mass spectrometer. Analytical procedure  
163 followed that of Tapster et al. (2016) and was corrected for  $^{230}\text{Th}$  disequilibrium using an assumed  
164 host Th/U composition of 1.43 (Simons et al., 2017). Uncorrected ages are reported in Electronic  
165 Appendix 3.

166 Zircon trace element analysis used the same instrumentation as LA-ICP-MS geochronology,  
167 normalized to NIST-612. Thirty  $\mu\text{m}$  spots were ablated on select zircon grains adjacent to previous  
168 ablation sites, measuring  $^{29}\text{Si}$ ,  $^{31}\text{P}$ ,  $^{39}\text{K}$ ,  $^{42}\text{Ca}$ ,  $^{45}\text{Sc}$ ,  $^{49}\text{Ti}$ ,  $^{51}\text{V}$ ,  $^{55}\text{Mn}$ ,  $^{89}\text{Y}$ ,  $^{91}\text{Zr}$ ,  $^{93}\text{Nb}$ ,  $^{118}\text{Sn}$ ,  $^{122}\text{Sb}$ ,  $^{133}\text{Cs}$ ,  $^{139}\text{La}$ ,  
169  $^{140}\text{Ce}$ ,  $^{141}\text{Pr}$ ,  $^{146}\text{Nd}$ ,  $^{147}\text{Sm}$ ,  $^{153}\text{Eu}$ ,  $^{157}\text{Gd}$ ,  $^{159}\text{Tb}$ ,  $^{163}\text{Dy}$ ,  $^{165}\text{Ho}$ ,  $^{167}\text{Er}$ ,  $^{169}\text{Tm}$ ,  $^{173}\text{Yb}$ ,  $^{175}\text{Lu}$ ,  $^{178}\text{Hf}$ ,  $^{182}\text{W}$ ,  $^{208}\text{Pb}$ ,  
170  $^{209}\text{Bi}$ ,  $^{232}\text{Th}$  and  $^{238}\text{U}$  (see Electronic Appendix 1). Analysis was internally standardized to stoichiometric  
171  $\text{SiO}_2$  concentrations (15.3 Si). NIST-610 (using reported concentrations from Pearce et al., 1997), and  
172 91500 (Wiedenbeck et al., 1995) and GJ-1 were used as secondary standards. Most elements were

173 within 10% of their reference composition and Gd, Tb and U are within 20% (see Electronic Appendix  
174 4).

## 175 4. Petrology and Geochemistry

### 176 4.1 Major and accessory mineralogy

177 All granites are porphyritic, with phenocrysts of quartz (8-25 mm) and perthitic orthoclase (10-40  
178 mm) within a fine-grained groundmass of plagioclase, tourmaline, and mica (Table 1). The granites of  
179 Crownhill can be divided into three types: (i) biotite (BG), (ii) tourmaline (TG) and (iii) two-mica  
180 granites. Each has been subjected to variable degrees of kaolinization and no fresh outcrops of the  
181 two-mica granite were located. The granites of Lee Moor are similar to the Crownhill TG, although  
182 with greater quartz and muscovite. The BG collected from Blackenstone Quarry is analogous to those  
183 collected from Crownhill, with less modal muscovite.

184 The BGs form a continuum of decreasing plagioclase content from Blackenstone to Crownhill,  
185 while orthoclase and quartz (CIPW normative) contents systematically increase (Figure 3a-b). The  
186 Crownhill TGs plot within the alkali feldspar granite field, on a QAP diagram whereas the Lee Moor  
187 TGs straddle the boundary between quartz-rich and alkali feldspar granite. Minor tourmaline veinlets  
188 are seen traversing through BG outcrops, yet no interstitial groundmass tourmaline has been  
189 observed. TGs host significant proportions of interstitial tourmaline (Figure 3c). Tourmaline also exists  
190 as isolated, euhedral crystals within the TGs with sector zoning (Figure 3d), sometimes with dark blue  
191 rims (e.g., Drivenes et al., 2015). Accessory cassiterite ( $\text{SnO}_2$ ) occurs exclusively within TGs as distinct  
192 clusters which are spatially associated with interstitial tourmaline (Figure 3e).

### 193 4.2 Zircon characteristics

194 Euhedral zircon grains in the groundmass of all granite types, mostly range from 50 to 300  $\mu\text{m}$  in  
195 length. They are found at the boundaries between crystal faces, as well as within fractures in  
196 phenocrysts and cleavage planes of micas (Figure 3f). Electron microscopy reveals consistent complex



197 zoning, and the cores of the Crownhill BG and TG zircon grains preserve remnants of oscillatory  
198 zoning that have been variably resorbed and fractured (Figure 3g). These zircon grains also have  
199 oscillatory-zoned rims that are up to 30  $\mu\text{m}$  in thickness. A few zircon grains possess an encasing  
200 metamict crust that is restricted to  $<20 \mu\text{m}$  in thickness (Figure 3h). All zircon cores incorporate  
201 apatite inclusions, which are not observed in the rims. The rims preserve a diverse inclusion  
202 assemblage of monazite (5-50  $\mu\text{m}$ ), xenotime ( $<10 \mu\text{m}$ ), uraninite, thorite, arsenopyrite, cinnabar,  
203 galena, chalcopyrite, and wolframite.

#### 204 4.3 Whole-rock major and trace elements

205 All samples are peraluminous, with  $>70 \text{ wt.}\% \text{ SiO}_2$ , which generally increases from BG to TG (see  
206 Supplementary Table 1).  $\text{Al}_2\text{O}_3$  exceeds 16 wt.% in the granites from Lee Moor. Conversely,  $\text{Na}_2\text{O}$ ,  
207  $\text{MgO}$ ,  $\text{TiO}_2$ ,  $\text{Fe}_2\text{O}_3$ ,  $\text{P}_2\text{O}_5$  and  $\text{CaO}$  mostly decrease from BG to the muscovite-bearing granites (Figure  
208 4a). A possible geochemical continuum exists between the BGs and TGs from Crownhill, whereas no  
209 clear trends exist in the Lee Moor samples. All samples display similar major element chemistry to  
210 previous studies (e.g., Charoy, 1986; Chappell & Hine, 2006; Simons et al., 2016). Blackenstone BG  
211 represent the least evolved of the studied granites, with the lowest  $\text{SiO}_2$ ,  $\text{Al}_2\text{O}_3$  and LOI as well as the  
212 highest  $\text{MgO}$ ,  $\text{FeO}$ ,  $\text{TiO}_2$  and  $\text{CaO}$ ; this geochemical signature is similar to that reported by Stone  
213 (1992; Figure 4b). As Figure 4 shows the BG at Crownhill has slightly more evolved compositions than  
214 the Blackenstone BG, with higher  $\text{SiO}_2$ ,  $\text{K}_2\text{O}$  and lower incompatible elements. Biotite granites  
215 consistently plot above the zirconium saturation threshold for peraluminous granites at  $750^\circ\text{C}$  ( $>100$   
216 ppm) of Watson & Harrison (1983), indicating that saturation concentrations are greater in the BGs  
217 (Figure 4c).

218 Tourmaline granites from both Crownhill and Lee Moor consistently represent the most  
219 evolved samples with the highest abundances of  $\text{Al}_2\text{O}_3$ ,  $\text{K}_2\text{O}$  and  $\text{Rb}$ , due to an increase in muscovite  
220 (Figure 4d). All BGs have broadly similar  $\text{Zr}$  concentrations and variable  $\text{Nb}$  concentrations.  $\text{TiO}_2$

221 against Nb/Ta depicts a curvilinear trend, where Nb/Ta ratios increase from TGs towards  
222 Blackenstone BG, which is the least differentiated sample.

223 All samples are LREE-enriched up to 100x chondrite values, with low Gd/Yb ratios and  
224 pronounced negative Eu anomalies (Figure 4g-h), similar to those obtained from other studies  
225 (Chappell & Hine, 2006; Simons et al., 2016). Crownhill BG show identical REE trends to the  
226 Blackstone BG, which comprises the largest  $\Sigma$ REE contents, the shallowest Eu anomaly ( $0.54 \pm 0.10$ )  
227 and lowest Gd/Yb<sub>CN</sub> ratio (1.28). Crownhill BGs display an overall, more evolved trend, with more  
228 pronounced Eu anomalies ( $0.36 \pm 0.10$ ). Crownhill TG possesses a similar geochemical trend to BG,  
229 despite large LREE variability ascribed to the combined effects of tourmalinization and argillic  
230 alteration (e.g., Alderton et al., 1980). The HREE trends are almost identical, yet with greater scatter  
231 (Gd/Yb<sub>CN</sub> ranging from 1.29 to 2.83). Lee Moor TGs possess the lowest  $\Sigma$ REE contents (see Electronic  
232 Appendix 3).

## 233 5. Integrated zircon analyses

### 234 5.1 LA-ICP-MS U-Pb geochronology

235 A total of seventy-seven zircon U-Pb measurements were made by LA-ICP-MS of which, thirty-three  
236 targeted resorbed zircon cores and forty-four targeted oscillatory-zoned rims from both the BG and  
237 TG. All ages are reported in Supplementary Table 2 and further information provided in Electronic  
238 Appendix 3.

239 From eighteen analyses, nine concordant analyses were obtained from resorbed zircon cores  
240 from the BG, yielding a weighted average  $^{238}\text{U}/^{206}\text{Pb}$  age of  $289 \pm 5$  Ma ( $2\sigma$ ; Figure 5a-b). Nine  
241 discordant analyses were omitted due to the ablation of compromised sectors of zircon grains,  
242 identified during post-ablation back-scattered electron observational study (i.e., rim-core mixing,  
243 fracturing, and inclusions). Oscillatory-zoned rims were typically thin ( $< 30 \mu\text{m}$ ) and zircon grains with  
244 rims exceeding the diameter of the ablation pit (10-15  $\mu\text{m}$ ) were selected for further analysis. From

245 twenty-eight analyses, nine concordant analyses were obtained from zircon rims of BG, yielding a  
246 weighted average  $^{238}\text{U}/^{206}\text{Pb}$  age of  $276 \pm 6$  Ma. Nineteen analyses were omitted due to recent Pb-loss  
247 and the ablation of compromised sectors of zircon grains, including metamictization.

248 The same methodology was performed on zircon grains from TG. From fifteen analyses,  
249 eleven concordant analyses yielded a weighted average age within uncertainty of BG zircon cores of  
250  $286 \pm 5$  Ma (Figure 5a-c). For oscillatory-zoned rims, eight concordant analyses were obtained from  
251 sixteen analyses, yielding a weighted average age of  $277 \pm 5$  Ma. Uranium concentrations are variable  
252 between the resorbed cores and the oscillatory-zoned rims of both suites, reaching up to 6,470 ppm  
253 in the cores and 8,170 ppm in the rims. Thorium/U values of zircon cores ranges from 0.03 to 0.81,  
254 whereas rims range from 0.02 to 0.03, with two anomalous values of 0.72 and 0.80.

255 Homogeneous monazite inclusions (5-40  $\mu\text{m}$ ) embedded within zircon rims were ablated in  
256 an attempt to further constrain the inferred two phases of magmatism. Only four concordant  
257 analyses were obtained from monazite inclusions in zircon from BGs (see Supplementary Table 3).  
258 Acquired dates spanned ages from both zircon cores and rims at  $280.0 \pm 11$  Ma (Figure 6).

## 259 5.2 CA-ID-TIMS U-Pb geochronology

260 The full dataset is reported in Electronic Appendix 3, with the data displayed in Supplementary Table  
261 4. Zircon dates obtained from LA-ICP-MS are consistent with geochronological data derived from CA-  
262 ID-TIMS analysis of crystal tips from Crownhill BG (n=6) and TG and all uncertainties are presented at  
263  $2\sigma$  level (n=4; Figure 5d-e). Uncertainties are presented as  $\pm$  analytical uncertainty/tracer  
264 calibration/decay constant. Seven concordant analyses derived from BG zircon grains yielded  $^{206}\text{Pb}/$   
265  $^{238}\text{U}$  ages ranging from 277.58 to 279.27 Ma. Calculated weighted mean ages generate  $277.74 \pm$   
266  $0.10/0.15/0.33$  Ma (n=4, MSWD=0.65). Model Th/U ratios range from 0.089 to 0.450 and are  
267 calculated based on the assumed concordancy between the U-Pb and Th-Pb systems. Four  
268 concordant analyses were obtained from TG zircon grains, possessing a  $^{206}\text{Pb}/^{238}\text{U}$  age range of  
269 278.09 to 279.34 Ma. A Devonian age of 383.99 Ma was also obtained from one fragment; however,

270 this was not reproduced from other analyses. The weighted mean age for TG is  $278.35 \pm$   
271  $0.14/0.19/0.35$  (n=3, MSWD=0.52), excluding the Devonian zircon. Th/U ratios for Permian ages  
272 samples are consistent, ranging from 0.12 to 0.25, whereas, the Devonian sample possesses a Th/U  
273 ratio of 1.1. Through combining the results from the two methodologies, two ages groups are  
274 apparent, where the 290-285 Ma group correlate with ages from two-mica and muscovite granites,  
275 such as Hemerdon and Bodmin, whereas the 280-275 Ma group correlates with BGs, such as  
276 Dartmoor and St. Austell (Chesley et al., 1993; Chen et al., 1993).

### 277 5.3 LA-ICP-MS trace element analysis

278 Cores from BG (n=22) have variably high U (184 to 4,000 ppm) and Th (77 to 618 ppm)  
279 concentrations, possessing Th/U ratios ranging from 0.038 to 0.810. Hafnium concentrations range  
280 from 7,440 to 12,080 ppm (Figure 7a). TG cores (n=19) possess similar U values to BG cores, yet Th  
281 values do not exceed 352 ppm, and so Th/U ratios display a smaller range from 0.017 to 0.289.  
282 Thorium decreases systematically with increasing Hf, grading from cores to rims, with BG rims (n=6)  
283 comprising Th/U ratios from 0.014 to 0.111 and Hf concentrations of 10,880 to 13,230 ppm. TG rims  
284 mirror these values, yet with Hf peaking at 16,600 ppm. Scatter exists in the data due to analytical  
285 precision and natural variation within a small dataset (see Supplementary Table 5).

286 Scandium against Th/U (Figure 7b) shows a curvilinear relationship between the granite suites  
287 (BG to TG) and their respective cores and rims. Biotite granite cores range from 100 to 462 ppm,  
288 which increases to TG cores with values from 141 to 629 ppm. Scandium begins to increase  
289 exponentially with decreasing Th/U, with BG rims peaking at 1,210 ppm and TG rims at 1,470 ppm.  
290 This pattern is observed in other trivalent elements (Y, Sb, Bi and LREEs) and W, but not Sn, which is  
291 depleted in all but a few BG cores. Using the equation derived by Watson et al. (2006), the  
292 temperature of zircon crystallisation can be estimated as  $(5080/(6.01\text{Log}(Ti_{zrn}))-273)$ , based on the  
293 isovalent substitution of  $Si^{4+}$  cations by  $Ti^{4+}$ . Biotite granite zircon cores retain a crystallisation  
294 temperature range of 710 to 875°C (analyses with <5 ppm Ti were discounted as they are below

295 detection limit), whereas TG cores range from 712 to 757°C. The calculated temperatures for the rims  
296 overlap with their respective cores.

297 Niobium and Ta values of zircon cores increase from BG to TG, whereas zircon rims possess  
298 variable concentrations of each element (Figure 7c). Nb/Ta ratios in BG cores range from 1.27 to 3.50,  
299 whereas TG cores peak at 11.24. Rim concentrations mirror those of their core counterpart, indicative  
300 of Nb-enrichment in select TG zircon grains. Zircon grains display characteristic REE trends, with LREEs  
301 in all analysed zircon domains ranging from 0.05 to 11 times that of chondritic values (Figure 7e-f).  
302 Rim  $\Sigma$ REEs are broadly more enriched relative to chondrites than zircon cores; however, have less  
303 prominent Ce and Eu anomalies. Biotite granite zircon rims have the lowest Ce/Ce\* values at 0.96 to  
304 1.79, with one anomalous value at 4.51, whereas their cores have Ce/Ce\* ratios up to 10.26, with two  
305 anomalous values at 27 to 30. Tourmaline granite zircon grains mirror this trend yet are broadly more  
306 enriched. Europium anomalies for cores average at  $0.08 \pm 0.05$ , whereas rims peak at 0.11 and 0.16  
307 for BGs and TGs, respectively. All samples show HREE enrichment ( $La/Yb_{CN} < 0.00561$ ). Gd/Yb<sub>CN</sub> ratios  
308 prove further HREE enrichment between granite suites and their respective zircon domains (Figure  
309 7d). Zircon cores from BGs range from Gd/Yb<sub>CN</sub> values of 0.054 to 0.229. Those from TG all reside  
310  $< 0.1$ . Zircon rims from BGs and TGs continue this trend, where TGs form the base at 0.03 (Gd/Yb<sub>CN</sub>;  
311 see Electronic Appendix 4).

## 312 6. Discussion

### 313 6.1 Age and origin of the Crownhill stock

314 Although the granites of the Cornubian Batholith are classified as S-type, significant zircon inheritance  
315 was not recorded in this study, allowing precise U-Pb zircon dating of even the most evolved granites  
316 in the batholith (e.g., Tapster et al., 2017). Negligible zircon inheritance can only be explained by the  
317 source rock being devoid of detrital zircon, as if all refractory zircon was consumed at the source,  
318 greater whole-rock Zr concentrations would be expected (Watson & Harrison, 1983). LA-ICP-MS and  
319 CA-ID-TIMS analyses collected for this study are in broad agreement, where the fragmented zircon

320 tips correlate with the ablated zircon rims from both granite populations. Zircon cores were only  
321 analysed by laser ablation due to the fragmenting technique adopted prior to CA-ID-TIMS analysis.

322 Laser analysis of zircon cores yielded  $288.9 \pm 5$  Ma and  $286.4 \pm 5$  Ma for BGs and TGs,  
323 respectively. These dates from the Crownhill stock and Lee Moor broadly correlate with granites at  
324 Bodmin Moor ( $291.4 \pm 0.8$  Ma; Chesley et al., 1993), Carnmenellis ( $293.7 \pm 0.6$  Ma; Chesley et al.,  
325 1993) and other two-mica and muscovite granites dated in the batholith (e.g., Carnmenellis and Carn  
326 Brea). Zircon rims from BG and TG yield ages of  $275.9 \pm 2.3$  Ma and  $277.6 \pm 1.7$  Ma, respectively,  
327 correlating with biotite granites, including those exposed at Dartmoor and Land's End (280 to 275 Ma;  
328 Chesley et al., 1993). However, these separate phases are not resolvable using LA-ICP-MS. The CA-ID-  
329 TIMS U-Pb geochronological analysis of zircon tip fragments corroborates the notion of a two-phase  
330 magmatic model, yielding ages of  $277.74 \pm 0.33$  Ma and  $278.35 \pm 0.35$  Ma for BG and TG,  
331 respectively. These ages replicate those produced from LA-ICP-MS analysis, whilst reducing the  
332 uncertainty, making these two phases temporally resolvable. U-Pb geochronology of zircon from the  
333 two-mica granite at Crownhill was hampered by the degree of crystal deformation and  
334 metamictisation subjected to the crystal.

335 The zircon cores derive from older two-mica and muscovite granites. These were likely  
336 sourced from granites that comprise the Crownhill two-mica and (or) Hemerdon muscovite granites,  
337 somewhere along the migration pathway of the second phase of magmatism. Upon entrainment  
338 within the BGs, assimilated zircon were resorbed and acted as a nucleation site for the crystallisation  
339 of zircon rims, creating the poly-phase architecture observed in the grains at Crownhill (Figure 8a).  
340 This further supports the model of two-stage granite magmatism and records the first evidence from  
341 the Cornubian Batholith for zircon inheritance between the two inferred granite phases. Crownhill  
342 represents one of the only localities in the batholith where two-mica and biotite granites occur  
343 adjacent to each other. Therefore, the assimilation of the former by the latter may not be  
344 documented elsewhere in the batholith. Moreover, throughout all analyses carried out in this study,

345 TGs produced the same geochemical and geochronological results as BGs, suggesting a common  
346 origin.

347 Whole-rock geochemistry indicates that the granites exposed at Crownhill are more evolved  
348 than those that comprise the Dartmoor pluton (higher SiO<sub>2</sub>, Al<sub>2</sub>O<sub>3</sub>, LILEs, HFSEs). Tourmaline granites  
349 across the batholith, occur in association with BGs. The formation of these granites is ascribed to the  
350 concentration of boron in the apical parts of a magma chamber, eventually forming a hydrous  
351 borosilicate phase, co-existing with the silicate magma (Müller et al., 2006). This phase then intrudes  
352 the pluton, forming stocks, orbicules or pods of tourmaline-rich granite (Drivenes et al., 2015). The  
353 compositional and textural similarity between TGs exposed at Crownhill and elsewhere in the  
354 batholith (e.g., St Austell and Land's End), suggests a similar emplacement model.

355 Trace elements in zircon suggest that the rims crystallised from a more evolved magma  
356 (greater Hf, Ta, Y), derived from a second episode of melting of a similar source rock. Zircon grains in  
357 tourmaline granites are broadly more evolved than those from BG. The apical parts of the magma  
358 chamber would have heightened concentrations of boron, which would increase the solubility of  
359 zircon and REE-phosphate and delay zircon fractionation (Charoy & Noronha, 1996; Breiter et al.,  
360 2006). Given sufficient fractionation, boron would eventually partition into the aqueous fluid phase,  
361 typically resulting in localised tourmalinisation, such as that observed at Crownhill (Pollard et al.,  
362 1987). Phosphorous and F would also concentrate in the fractionated apical portions of the magma  
363 chamber and increase the solubility of zircon (e.g., Keppler, 1993). Lithium would behave similarly,  
364 but have the opposite effect on zircon solubility (Linnen, 1998). At Crownhill and Lee Moor, Knox &  
365 Jackson (1990) report minor interstitial and pseudomorphic topaz and Li-mica within late-stage  
366 aplites, spatially associated with tourmaline veins and pods. This indicates that these elements  
367 concentrated together, where B partitioned into the co-existing aqueous fluid phase and F and P was  
368 retained in the fractionated melt, which was later expelled as aplitic intrusions (Pollard et al., 1987).  
369 Moreover, zircon rims sourced from the TG are consistently depleted in P (Supplementary Table 5),

370 perhaps as a result of co-crystallising apatite (London et al., 1988). The delayed fractionation of zircon  
371 is tentatively supported by the broadly lower crystallisation temperatures recorded in TG zircon cores,  
372 relative to BG.

## 373 6.2 Implications for Sn-W mineralisation

374 Tin-tungsten mineralisation spans the batholith both spatially and temporally. The older granite  
375 plutons and stocks are the most prospective for tungsten-dominated deposits (290 Ma; 401 Mt at  
376 0.13% W and 0.02% Sn; Chesley et al., 1993), Cligga Head (280 Ma; 3000 t W; Dines et al., 1956) and  
377 now the W-Sn-Cu Redmoor Prospect (284 Ma; 13.3 Mt at 0.16% W and 0.21% Sn; Chesley et al., 1993;  
378 New Age Exploration, 2018). Tin mineralisation typically occurs endogenically, in association with  
379 biotite and tourmaline granites. The W/Sn ratio remains broadly consistent across the granite types  
380 (see Shepherd et al., 1985), despite recent studies suggesting a temporal decoupling of these  
381 elements (Simons et al., 2017; Tapster et al., 2017). Wolframite is noted as the earliest mineralising  
382 phase in most paragenetic models in the Cornubian Batholith (Jackson et al., 1989). This suggests that  
383 W was predominantly liberated from the source during the first phase of granite magmatism,  
384 whereas, Sn was sequestered in a more refractory host (Romer & Kroner, 2016; Simons et al., 2017).  
385 Simons et al. (2017) propose that W is compatible within the muscovite lattice, capable of being  
386 liberated during dehydration melting at moderate temperatures and pressure (731-806°C, >5 kbar).  
387 Tin however, is concentrated in biotite, together with more refractory minerals, through the  
388 isomorphic replacement of  $Ti^{4+}$  ( $D_{0-2.32}$ ; Lehmann, 1982; Williamson et al., 2010), meaning it requires  
389 greater temperatures (>1000°C) to extract Sn from the source (Romer & Kroner, 2016).

390 Cassiterite mineralisation is closely associated tourmaline (Williamson et al., 2010 and this study)  
391 and fluorine (Chesley et al., 1993) across the Cornubian Batholith. At Crownhill, cassiterite is  
392 associated with tourmaline that display blue overgrowths, a texture ascribed to the crystallisation of a  
393 late aqueous fluid (Müller et al., 2005; Drivenes et al., 2015). The pseudomorphic replacement of  
394 biotite by tourmaline may have elevated the  $Sn^{4+}$  concentration of the borosilicate fluid, increasing



395 the likelihood of cassiterite crystallisation, potentially catalysed by the addition of oxidising meteoric  
396 fluids and/or formation waters (Shepherd et al., 1985; Walshe et al., 1996; Duchoslav et al., 2017). It  
397 has been experimentally determined that tourmaline replacing biotite would not liberate Sn to the  
398 fluid (Hosking, 1964; Alderton & Moore, 1981). However in reduced saline fluids, Sn is more  
399 incompatible with tourmaline ( $\ll 1,000$  ppm; Esmaeily et al., 2005; Williamson et al., 2010). Fluid  
400 inclusion work at Dartmoor (Rankin & Alderton, 1983; Alderton et al., 1992), suggests that the  
401 Dartmoor BGs were in equilibrium with high-saline fluid (30-50 wt.% NaCl eq.), which would have  
402 been capable of liberating Sn from biotite.

### 403 6.3 Comparison with Variscan Granites

404 Monazite and xenotime geochronometers have been used to date the emplacement of peraluminous  
405 granites, such as the Central Iberian Zone (CIZ; Valle Aguado et al., 2005), Bohemian Massif (Kusiak et  
406 al., 2014) and the French Massif Central (FMC; Laurent et al., 2017). Zircon cores have been often  
407 excluded due to metamictisation and inferred crustal inheritance. Zircon textures observed in the  
408 composite Crownhill stock (Figure 8) are similar to those of the FMC (Laurent et al., 2017) and the CIZ  
409 (Pereira et al., 2018), where zircon crystals possess resorbed xenocrystic cores derived from the  
410 granite protolith, overgrown by oscillatory-zoned rims that crystallised directly from the magma. Post-  
411 collisional granite plutonism in the CIZ (310-295 Ma) is also composed of two major magmatic pulses  
412 separated by a 5 Ma magmatic hiatus, ascribed to a delayed travel time of the thermal anomaly  
413 responsible for partial melting (Gutiérrez-Alonso et al., 2011; Teixeira et al., 2012). Díaz-Alvarado et al.  
414 (2016) supports this model by dating poly-phase zircon crystals from the CIZ. These zircon crystals are  
415 interpreted to comprise a resorbed antecrystic core derived from the earlier phase of granite  
416 magmatism, overgrown by a zircon rim 5 Ma younger within the later phase.

417 Incompatible fluxing elements (e.g., B, F, P) concentrate in the residual magma during  
418 fractional crystallisation (Černý et al., 2005). From this, zircon solubility increases, which delays zircon  
419 fractionation and results in a more evolved (greater Hf, Ta and Y) final composition (i.e., the Podlesí

420 granite, Czech Republic, Breiter et al., 2006; Breiter et al., 2016). Cassiterite often crystallises in  
421 association with tourmaline derived from exsolved magmatic fluids in highly evolved granites,  
422 sometimes together with topaz and Li-mica (Erzgebirge, Štemprok & Blecha, 2015; Western  
423 Carpathian granites, Broska & Kubiš, 2018; CIZ, Roda-Robles et al., 2018). This is observed in the  
424 Cornubian Batholith (this study and Duchoslav et al., 2017), where cassiterite precipitation is  
425 predominantly governed by the redox state of the host fluid. Biotite can readily host Sn<sup>4+</sup> (Romer &  
426 Kroner, 2016; Simons et al., 2017), where Chen et al. (2013) proposes that chloritization of biotite can  
427 leach Sn to form cassiterite, however, it is unclear whether tourmalinization can have the same effect.  
428 The isovolumetric replacement of biotite by tourmaline is also noted in the Penamacor-Monsato  
429 pluton of the CIZ (Da Costa et al., 2014), yet no cassiterite is observed

## 430 7. Conclusions

431 The composite Crownhill stock represents the only stock in the Cornubian Batholith that is composed  
432 of two-mica, biotite, and tourmaline granite. Both LA-ICP-MS and CA-ID-TIMS U-Pb geochronology of  
433 poly-phase zircon grains liberated from the biotite and tourmaline granites of Crownhill and Lee Moor  
434 support a two-phase magmatic model. Zircon cores yield an age range of 290-288 Ma consistent with  
435 older granite plutons (e.g., Bodmin and Carnmenellis), whereas, the corresponding rims yield ages of  
436 278-276 Ma that correlate with younger plutons (e.g., Dartmoor and Land's End). From these ages,  
437 we propose that zircon cores crystallised from the initial phase of granite magmatism, to then be  
438 assimilated and incorporated into the second phase, which was responsible for crystallising the rims.  
439 Trace element data from zircon cores and rims indicate that the rims crystallised from a more evolved  
440 magma, where those sampled from tourmaline granites are broadly more evolved than those from  
441 biotite granites. This suggests that zircon fractionation was delayed in the tourmaline granites, likely  
442 as a result of the increased solubility of zirconium in a volatile-rich portion of a magma chamber. The  
443 interaction of borosilicate fluids with antecedent biotite granites could perhaps have triggered the

444 pseudomorphic replacement of biotite by tourmaline. This process could be responsible for liberating  
445 Sn from the biotite and henceforth, facilitating the precipitation of cassiterite.

446

#### 447 **Acknowledgements**

448 This work was supported by the Society of Economic Geologists Hugh E. McKinstry Grant with further  
449 support from the Mineralogical Society of Great Britain and Ireland research bursary. W.D.S  
450 acknowledges the University of Portsmouth Postgraduate Scholarship Scheme. J.R.D acknowledges a  
451 Higher Education Innovation Fund grant and Researcher Development Fund grant from the University  
452 of Portsmouth. The authors thank Wolf Minerals and Sibelco for providing samples, supplementary  
453 data and site access. Academic and technical staff at UoP are acknowledged for advice and help  
454 during sample preparation and analytical procedures, particularly Joe Dunlop and Mike Fowler. Bruno  
455 Dhuime is thanked for his assistance during mineral separation at the University of Bristol. Richard  
456 Scrivener is thanked for his guidance and advice throughout the project. Andrew Kerr, Beth Simons,  
457 and one anonymous reviewer are thanked for their constructive comments that greatly improved the  
458 manuscript. Nelson Eby and Michael Roden are thanked for their editorial handling.

#### 459 **References**

460 Aguado, B. V., Azevedo, M. R., Schaltegger, U., Catalán, J. M., & Nolan, J. (2005). U–Pb zircon and  
461 monazite geochronology of Variscan magmatism related to syn-convergence extension in Central  
462 Northern Portugal. *Lithos*, 82(1-2), pp. 169-184.

463 Alderton, D. H., Rankin, A. H., & Thompson, M. (1992). Fluid inclusion chemistry as a guide to tin  
464 mineralization in the Dartmoor granite, south-west England. *Journal of Geochemical*  
465 *Exploration*, 46(2), pp. 163-185.

466 Alderton, D. H. M., & Moore, F. (1981). New determinations of tin and tungsten in granites from  
467 south-west England. *Mineralogical Magazine*, 44(335), pp. 354-356.

468 Alderton, D. H. M., Pearce, J. A., & Potts, P. J. (1980). Rare earth element mobility during granite  
469 alteration: evidence from southwest England. *Earth and Planetary Science Letters*, 49(1), pp. 149-165.

470 Beer, K., & Scrivener, R. (1982). Metalliferous mineralisation. In L. D. Durrance E.M. (Ed.). *The geology*  
471 *of Devon* (p. 117-147). University of Exeter.

472 Black, L. P., Kamo, S. L., Allen, C. M., Davis, D. W., Aleinikoff, J.N, J. N., Valley, J. W., Mundil, R.,  
473 Campbell, I.H., Korsch, R.J., Williams, I.S. & Foudoulis, C. (2004). Improved  $^{206}\text{Pb}/^{238}\text{U}$  microprobe  
474 geochronology by the monitoring of a trace-element-related matrix effect; SHRIMP, ID-TIMS, ELA-ICP-  
475 MS and oxygen isotope documentation for a series of zircon standards. *Chemical Geology*, 205(1-2),  
476 pp. 115-140.

477 Bott, M. H. P., Day, A. A., & Masson-Smith, D. (1958). The geological interpretation of gravity and  
478 magnetic surveys in Devon and Cornwall. *Phil. Trans. R. Soc. Lond. A*, 251(992), pp. 161-191.

479 Boynton, W. V. (1985). Chapter 3. Cosmochemistry of the rare earth elements: Meteorite studies. In  
480 P. Henderson, *Rare Earth Element Geochemistry*, pp. 115-1522.

481 Breiter, K., Müller, A., Shail, R., & Simons, B. (2016). Composition of zircon grains from the Cornubian  
482 Batholith of SW England and comparison with zircon grains from other European Variscan rare-metal  
483 granites. *Mineralogical Magazine*, 80(7), pp. 1273-1289.

484 Breiter, K., Förster, H. J., & Škoda, R. (2006). Extreme P-, Bi-, Nb-, Sc-, U- and F-rich zircon from  
485 fractionated perphosphorous granites: The peraluminous Podlesí granite system, Czech  
486 Republic. *Lithos*, 88(1-4), pp. 15-34.

487 Broska, I., & Kubiš, M. (2018). Accessory minerals and evolution of tin-bearing S-type granites in the  
488 western segment of the Gemeric Unit (Western Carpathians). *Geologica Carpathica*, 69(5), pp. 483-  
489 497.

490 Chadwick, R. A., & Evans, D. J. (1995). The timing and direction of Permo-Triassic extension in  
491 southern Britain. *Geological Society Special Publication*, 91, pp. 161-192.

492 Chappell, B. W., & Hine, R. (2006). The Cornubian Batholith: An example of magmatic fractionation on  
493 a Crustal Scale. *Resource Geology*, 56(3), pp. 203-244.

494 Charoy, B. (1986). The Genesis of the Cornubian Batholith (South-West England): the example of the  
495 Carnmenellis Pluton. *Journal of Petrology*, 27(3), pp. 571-604.

496 Charoy, B., Noronha, F. (1996); Multistage Growth of a Rare-Element, Volatile-Rich Microgranite at  
497 Argemela (Portugal), *Journal of Petrology*, 37(1), pp. 73–94.

498 Chen, Y., Clark, A. H., Farrar, E., Wasteneys, H. A., Hodges on, M. J., & Bromley, A. V. (1993).  
499 Diachronous and independent histories of plutonism and mineralisation in the Cornubian Batholith,  
500 southwest England. *Journal of the Geological Society of London*, 150, pp. 1183-1191.

501 Chen, J., Wang, R., Zhu, J., Lu, J., & Ma, D. (2013). Multiple-aged granitoids and related tungsten-tin  
502 mineralization in the Nanling Range, South China. *Science China Earth Sciences*, 56(12), pp. 2045-  
503 2055.

504 Chesley, J. T., Halliday, A. N., See, L. W., Meager, K., Shepherd, T. J., & Scrivener, R. C. (1993).  
505 Thermochronology of the Cornubian Batholith in southwest England: Implications for pluton  
506 emplacement and protracted hydrothermal mineralisation. *Geochimica et Cosmochimica Acta*, 57,  
507 pp. 1817-1835.

508 Clark, A. H., Chen, Y., Farrar, E., Wasteneys, H. A., Stimac, J. A., & Hodgson, M. J. (1993). The  
509 Cornubian Sn-Cu (-As, W) Metallogenic Province: Product of a 30My History of discrete and  
510 concomitant anatectic, intrusive and hydrothermal events. *Proceedings of the Ussher Society*, 8, pp.  
511 112-116.

512 Černý, P., Blevin, P.L., Cuney, M., London, D (2005). Granite-related ore deposits. *Society of Economic*  
513 *Geologists*, 100th Anniversary, pp. 337-370.

514 Da Costa, I. R., Mourão, C., Récio, C., Guimarães, F., Antunes, I. M., Ramos, J. F., ... & Milton, J. A.  
515 (2014). Tourmaline occurrences within the Penamacor-Monsanto granitic pluton and host-rocks

516 (Central Portugal): genetic implications of crystal-chemical and isotopic features. Contributions to  
517 Mineralogy and Petrology, 167(4), pp. 993.

518 Dangerfield, J., & Hawkes, J. R. (1981). The Variscan granites of south-west England: additional  
519 information. Proceedings of the Ussher Society, 5, pp. 116-120.

520 Darbyshire, D. P., & Shepherd, T. J. (1985). Chronology of granite magmatism and associated  
521 mineralisation, SW England. Journal of the Geological Society of London, 142, pp. 1159-1177

522 Darbyshire, D.P.F., Shepherd, T.J. (1987). Chronology of magmatism in south-west England: the minor  
523 intrusions. Proceedings of the Ussher Society, 6, pp. 431-438.

524 Dines, H.G., 1956. The metalliferous mining region of south-west England. Volume 1. HM Stationery  
525 Office.

526 Díaz-Alvarado, J., Fernández, C., Chichorro, M., Castro, A., & Pereira, M. F. (2016). Tracing the  
527 Cambro-Ordovician ferrosilicic to calc-alkaline magmatic association in Iberia by in situ U–Pb SHRIMP  
528 zircon geochronology (Gredos massif, Spanish Central System batholith). Tectonophysics, 681, pp. 95-  
529 110.

530 Drivenes, K., Larsen, R. B., Müller, A., Sørensen, B. E., Wiedenbeck, M., & Raanes, M. P. (2015). Late-  
531 magmatic immiscibility during batholith formation: assessment of B isotopes and trace elements in  
532 tourmaline from the Land's End granite, SW England. Contributions to Mineralogy and  
533 Petrology, 169(6), pp. 56.

534 Duchoslav, M., Marks, M. A. W., Drost, K., McCammon, C., Marschall, H. R., Wenzel, T., & Markl, G.  
535 (2017). Changes in tourmaline composition during magmatic and hydrothermal processes leading to  
536 tin-ore deposition: The Cornubian Batholith, SW England. Ore Geology Reviews, 83, pp. 215-234.

537 Dupuis, N. E., Braid, J. A., Murphy, J. B., Shail, R. K., Archibald, D. A., & Nance, R. D. (2015).  $^{40}\text{Ar}/^{39}\text{Ar}$   
538 phlogopite geochronology of lamprophyre dykes in Cornwall, UK: new age constraints on Early

539 Permian post-collisional magmatism in the Rhenohercynian Zone, SW England. *Journal of the*  
540 *Geological Society*, pp. 2014-151.

541 Esmaeily, D., Nédélec, A., Valizadeh, M. V., Moore, F., & Cotten, J. (2005). Petrology of the Jurassic  
542 Shah-Kuh granite (eastern Iran), with reference to tin mineralisation. *Journal of Asian Earth*  
543 *Sciences*, 25(6), 961-980.

544 Evans, J.A., 1989. Short Paper: A note on Rb-Sr whole-rock ages from cleaved mudrocks in the Welsh  
545 Basin. *Journal of the Geological Society*, 146(6), pp.901-904.

546 Exley, C. S., & Stone, M. (1982). Hercynian intrusive rocks. In D. S. Sutherland, *Igneous Rocks of the*  
547 *British Isles*, pp. 287-320.

548 Franke, W., Haak, V., Oncken, O., & Tanner, D. (2000). Orogenic processes: quantification and  
549 modelling in the Variscan belt. *Geological Society, London, Special Publications*, 179(1), pp. 1-3.

550 Gonçalves, G.O., Lana, C., Scholz, R., Buick, I.S., Gerdes, A., Kamo, S.L., Corfu, F., Marinho, M.M.,  
551 Chaves, A.O., Valeriano, C. and Nalini Jr, H.A., 2016. An assessment of monazite from the Itambé  
552 pegmatite district for use as U–Pb isotope reference material for microanalysis and implications for  
553 the origin of the “Moacyr” monazite. *Chemical Geology*, 424, pp. 30-50.

554 Guillong, M., Meier, D. L., Allan, M. M., Heinrich, C. A., & Yardley, B. W. (2008). SILLS: a MATLAB-based  
555 program for the reduction of laser ablation ICP-MS data of homogeneous materials and inclusions. In  
556 P. Sylvester, *Laser Ablation ICP-MS in the Earth Sciences: Current Practices and Outstanding Issues*,  
557 40, pp. 328-333. *Mineral Association of Canada: Short Course Series*.

558 Gutiérrez-Alonso, G., Fernández-Suárez, J., Jeffries, T.E., Johnston, S.T., Pastor-Galán, D., Murphy, J.B.,  
559 Franco, M.P, and Gonzalo, J.C (2011). Diachronous post-orogenic magmatism within a developing  
560 orocline in Iberia, European Variscides. *Tectonics*, 30(5), pp. 1-17.

561 Horstwood, M. S., Foster, G. L., Parrish, R. R., Noble, S. R., & Nowell, G. M. (2003). Common-Pb  
562 corrected in situ U–Pb accessory mineral geochronology by LA-MC-ICP-MS. *Journal of Analytical*  
563 *Atomic Spectrometry*, 18(8), pp. 837-846.

564 Hosking, K.F.G. (1964). Permo-Carboniferous and later mineralisation of Cornwall and south-west  
565 Devon in Hosking & Shrimpton (eds). *Present views of some aspects of the geology of Cornwall and*  
566 *Devon*. Pp. 201-245.

567 Imai, N., Terashima, S., Itoh, S., & Ando, A. (1995). 1994 compilation of analytical data for minor and  
568 trace elements in seventeen GSI geochemical reference samples, "Igneous rock series". *Geostandards*  
569 *Newsletter*, 19, pp. 135-213.

570 Isaac, K. P., Turner, P. J., & Stewart, I. J. (1982). The evolution of the Hercynides of central SW  
571 England. *Journal of the Geological Society of London*, 139, pp. 521-521.

572 Jackson, N. J., Willis-Richards, J., Manning, D. A., & Sams, M. S. (1989). Evolution of the Cornubian Ore  
573 Field, Southwest England: Part II. Mineral Deposits and Ore-Forming Processes. *Economic Geology*,  
574 84, pp. 1101-1133.

575 Jackson, S. E., Pearson, N. J., Griffin, W. L., & Belousova, E. A. (2004). The application of laser ablation-  
576 inductively coupled plasma-mass spectrometry to in situ U/Pb zircon geochronology. *Chemical*  
577 *Geology*, 211(1-2), pp. 47-69.

578 Keppler, H. (1993). Influence of fluorine on the enrichment of high field strength trace elements in  
579 granitic rocks. *Contributions to Mineralogy and Petrology*, 114(4), pp. 479-488.

580 Knox, D. A., & Jackson, N. J. (1990). Composite granite intrusions of SW Dartmoor, Devon. *Proceedings*  
581 *of the Ussher Society*, 7, pp. 246-251.

582 Kroner, U., & Romer, R. L. (2013). Two plates—many subduction zones: the Variscan orogeny  
583 reconsidered. *Gondwana Research*, 24(1), pp. 298-329.



584 Kusiak, M. A., Williams, I. S., Dunkley, D. J., Konečný, P., Słaby, E., & Martin, H. (2014). Monazite to the  
585 rescue: U–Th–Pb dating of the intrusive history of the composite Karkonosze pluton, Bohemian  
586 Massif. *Chemical Geology*, 364, pp. 76-92.

587 Laurent, O., Couzinié, S., Zeh, A., Vanderhaeghe, O., Moyen, J. F., Villaros, A., ... & Chelle-Michou, C.  
588 (2017). Protracted, coeval crust and mantle melting during Variscan late-orogenic evolution: U–Pb  
589 dating in the eastern French Massif Central. *International Journal of Earth Sciences*, 106(2), pp. 421-  
590 451.

591 Lehmann, B. (1982). Metallogeny of tin; magmatic differentiation versus geochemical  
592 heritage. *Economic Geology*, 77(1), pp. 50-59.

593 Leveridge, B., & Hartley, A. J. (2006). The Variscan Orogeny: the development and deformation of  
594 Devonian/Carboniferous basins in SW England and South Wales. In: *The geology of England and*  
595 *Wales*/edited by PJ Brenchley and PF Rawson. London: Geological Society of London, 2006, pp. 225-  
596 255.

597 Linnen, R. L. (1998). The solubility of Nb-Ta-Zr-Hf-W in granitic melts with Li and Li+ F; constraints for  
598 mineralization in rare metal granites and pegmatites. *Economic Geology*, 93(7), pp. 1013-1025.

599 London, D., Hervig, R. L., & Morgan, G. B. (1988). Melt-vapor solubilities and elemental partitioning in  
600 peraluminous granite-pegmatite systems: experimental results with Macusani glass at 200  
601 MPa. *Contributions to Mineralogy and Petrology*, 99(3), pp. 360-373.

602 MacRae, C., Wilson, N., Torpy, A., Pownceby, M., Hanchar, J., Davidson, C., & Hugo, V. (2014). Zircon  
603 metamictisation study by Cathodoluminescence and X-ray Imaging. *Microscopy and*  
604 *Microanalysis*, 20(S3), pp. 908-909.

605 Manning, D.A.C., Hill, P.I., Howe, J.H (1996). Primary lithological variation in the kaolinized St. Austell  
606 Granite, Cornwall, England. *Journal of the Geological Society*, 153, pp. 827-838.

607 Mattinson, J. M. (2005). Zircon U-Pb chemical abrasion ("CA-TIMS") method: Combined annealing and  
608 multi-step partial dissolution analysis for improved precision and accuracy of zircon ages. *Chemical*  
609 *Geology*, 220 (1-2), pp. 46-66.

610 Moreira, H., Seixas, L., Storey, C., Fowler, M., Lasalle, S., Stevenson, R., & Lana, C. (2018). Evolution of  
611 Siderian juvenile crust to Rhyacian high Ba-Sr magmatism in the Mineiro Belt, southern São Francisco  
612 Craton. *Geoscience Frontiers*, 9(4), pp. 977-995.

613 Müller, A., Seltmann, R., Halls, C., Siebel, W., Dulski, P., Jeffries, T., ... & Kronz, A. (2006). The  
614 magmatic evolution of the Land's End pluton, Cornwall, and associated pre-enrichment of metals. *Ore*  
615 *Geology Reviews*, 28(3), pp. 329-367.

616 Müller, A., & Halls, C. (2005). Rutile—the tin-tungsten host in the intrusive tourmaline breccia at  
617 Wheal Remfry, SW England. In *Mineral Deposit Research: Meeting the Global Challenge*, pp. 441-444.

618 Nance, R. D., Gutierrez-Alonso, G., Keppie, J. D., Linnemann, U., Murphy, J. B., Quesada, C., Strachan  
619 R.A., Woodcock, N. H. (2010). Evolution of the Rheic Ocean. *Gondwana Research*, 17, pp. 194-222.

620 Neace, E. R., Nance, R. D., Murphy, J. B., Lancaster, P. J., & Shail, R. K. (2016). Zircon LA-ICPMS  
621 geochronology of the Cornubian Batholith, SW England. *Tectonophysics*, 681, pp. 332–352.

622 New Age Exploration, Cornwall Resources Limited & SRK Exploration. (2018). Redmoor 2018 Mineral  
623 Resource Update.

624 Pearce, N. J. G., Perkins, W. T., Westgate, J. A., Gorton, M. P., Jackson, S. E. C., Neal, R., Chenery, S. P.  
625 (1997). A compilation of new and published major and trace element data for NIST SRM 610 and NIST  
626 SRM 612 glass reference materials, *Geostandards Newsletter*, 21, pp. 115–144.

627 Pereira, M. F., Castro, A., Fernández, C., & Rodríguez, C. (2018). Multiple Paleozoic magmatic-orogenic  
628 events in the Central Extremadura batholith (Iberian Variscan belt, Spain). *Journal of Iberian Geology*,  
629 pp. 1-25.

630 Pollard, P. J., Pichavant, M., & Charoy, B. (1987). Contrasting evolution of fluorine- and boron-rich tin  
631 systems. *Mineralium Deposita*, 22(4), pp. 315-321.

632 Rankin, A.H. & Alderton, D.H.M. (1983). Fluid Inclusion Petrography of SW England Granites and its  
633 Potential in Mineral Exploration. *Mineral Deposita* 18(2), pp. 335-347.

634 Roda-Robles, E., Villaseca, C., Pesquera, A., Gil-Crespo, P. P., Vieira, R., Lima, A., & Garate-Olave, I.  
635 (2018). Petrogenetic relationships between Variscan granitoids and Li-(FP)-rich aplite-pegmatites in  
636 the Central Iberian Zone: Geological and geochemical constraints and implications for other regions  
637 from the European Variscides. *Ore Geology Reviews*, 95, pp. 408-430.

638 Romer, R. L., & Kroner, U. (2016). Phanerozoic tin and tungsten mineralization—tectonic controls on  
639 the distribution of enriched protoliths and heat sources for crustal melting. *Gondwana Research*, 31,  
640 pp. 60-95.

641 Romer, R. L., Thomas, R., Stein, H. J., & Rhede, D. (2007). Dating multiply overprinted Sn-mineralized  
642 granites—examples from the Erzgebirge, Germany. *Mineralium Deposita*, 42(4), pp. 337-359.

643 Santos, M. M., Lana, C., Scholz, R., Buick, I., Schmitz, M. D., Kamo, S. L., Corfu, F., Tapster, S.,  
644 Lancaster, P., Storey, C.D., Basei, M.A.S., Tohver, E., Alkmim, A., Nalini, H., Krambrock, K., Fantini, C.,  
645 Wiedenbeck, M. (2017). A New Appraisal of Sri Lanka BB Zircon as a Reference Material for LA-ICP-  
646 MS U-Pb Geochronology and Lu-Hf Isotope Tracing. *Geostandards and Geoanalytical Research*, 41(3),  
647 pp. 335-358.

648 Shail, R. K., & Alexander, A. C. (1997). Late Carboniferous to Triassic reactivation of Variscan basement  
649 in the western English Channel: evidence from onshore exposures in south Cornwall. *Journal of the*  
650 *Geological Society*, 154, pp. 163-168.

651 Shail, R. K., & Wilkinson, J. J. (1994). Late-to Post-Variscan Extensional Tectonics in South Cornwall.  
652 *Proceedings of the Ussher Society*, 8, pp. 262-270.

653 Shail, R. K., & Leveridge, B. E. (2009). The Rheohercynian passive margin of SW England:  
654 Development, inversion and extensional reactivation. *Comptes Rendus Geoscience*, 341(2-3), pp. 140-  
655 155.

656 Shepherd, T. J., Miller, M. F., Scrivener, R. C., & Darbyshire, D. P. (1985). Hydrothermal fluid evolution  
657 in relation to mineralisation in southwest England with special reference to the Dartmoor-Bodmin  
658 area in High heat production (HHP) granites, hydrothermal circulation and ore genesis, 1, pp. 345-  
659 364.

660 Simons, B., Shail, R. K., & Anderson, J. C. (2016). The petrogenesis of the Early Permian Variscan  
661 granites of the Cornubian Batholith: Lower plate post-collisional peraluminous magmatism in the  
662 Rheohercynian Zone of SW England. *Lithos*, 260, pp. 76-94.

663 Simons, B., Anderson, J. C., Shail, R. K., & Jenner, F. (2017). Fractionation of Li, Be, Ga, Nb, Ta, In, Sn,  
664 Sb, W and Bi in the peraluminous Early Permian Variscan granites of the Cornubian Batholith:  
665 precursor processes to magmatic-hydrothermal mineralisation. *Lithos*, 278-281, pp. 491-512.

666 Sláma, J., Košler, J., Condon, D. J., Crowley, J. L., Gerdes, A., Hanchar, J. M., Whitehouse, M. J. (2009).  
667 Plešovice zircon — A new natural reference material for U–Pb and Hf isotopic microanalysis. *Chemical*  
668 *Geology*, 249, pp. 1-35.

669 Stacey, J. S., & Kramers, J. D. (1975). Approximation of Terrestrial Lead Isotope Evolution by a 2-Stage  
670 Model. *Earth and Planetary Science Letters*, 26(2), pp. 207-221.

671 Štemprok, M., & Blecha, V. (2015). Variscan Sn–W–Mo metallogeny in the gravity picture of the  
672 Krušné hory/Erzgebirge granite batholith (Central Europe). *Ore Geology Reviews*, 69, pp. 285-300.

673 Stone, M. (1992). The Tregonning granite: petrogenesis of Li-mica granites in the Cornubian  
674 batholith. *Mineralogical Magazine*, 56(383), pp. 141-155.

675 Sylvester, P. J. (1998). Post-collisional strongly peraluminous granites. *Lithos*, 45, pp. 29-44.

676 Tapster, S., Condon, D.J., Naden, J., Noble, S.R., Petterson, M.G., Roberts, N.M.W., Saunders, A.D. and  
677 Smith, D.J. (2016). Rapid thermal rejuvenation of high-crystallinity magma linked to porphyry copper  
678 deposit formation; evidence from the Koloula Porphyry Prospect, Solomon Islands. *Earth and*  
679 *Planetary Science Letters*, 442, pp.206-217.

680 Tapster, S., Shail, R. K., McAllister, H., Deady, E., & McFarlane, J. (2017). Understanding the multi-  
681 episode formation of the world-class Hemerdon W–Sn deposit in the context of SW England granite  
682 evolution. *Applied Earth Science*.

683 Taylor, G. K. (2007). Pluton shapes in the Cornubian Batholith: new perspectives from gravity  
684 modelling. *Journal of the Geological Society*, 164(3), pp. 525-528.

685 Teixeira, R. J. S., Neiva, A. M., Gomes, M. E. P., Corfu, F., Cuesta, A., & Croudace, I. W. (2012). The role  
686 of fractional crystallisation in the genesis of early syn-D3, tin-mineralized Variscan two-mica granites  
687 from the Carrazeda de Ansiães area, northern Portugal. *Lithos*, 153, pp. 177-191.

688 Walshe, J. L., Halley, S. W., Anderson, J. A., & Harrold, B. P. (1996). The interplay of groundwater and  
689 magmatic fluids in the formation of the cassiterite-sulfide deposits of western Tasmania. *Ore Geology*  
690 *Reviews*, 10(3-6), pp. 367-387.

691 Warr, L. N., Primmer, T. J., & Robinson, D. (1991). Variscan very low-grade metamorphism in  
692 southwest England: a diastathermal and thrust-related origin. *Journal of Metamorphic Geology*, 9(6),  
693 pp. 751-764.

694 Watson, E. B., & Harrison, T. M. (1983). Zircon saturation revisited: temperature and composition  
695 effects in a variety of crustal magma types. *Earth and Planetary Science Letters*, 64(2), pp. 295-304.

696 Watson, E. B., Wark, D. A., & Thomas, J. B. (2006). Crystallisation thermometers for zircon and rutile.  
697 *Contributions to Mineralogy and Petrology*, 151(4), pp. 413.

698 Wiedenbeck, M., Allé, P., Corfu, F., Griffin, W. L., Meier, M., Orbeli, F., Spiegel, W. (1995). Three  
699 natural zircon standards for U-Th-Pb, Lu-Hf, trace element and REE analyses. *Geostandards*  
700 *Newsletter*, 19, pp. 1-23.

701 Williams, M. L., Jercinovic, M. J., Harlov, D. E., Budzyn, B., & Hetherington, C. J. (2011). Resetting  
702 monazite ages during fluid-related alteration. *Chemical Geology*, 283(3-4), pp. 218-225.

703 Williamson, B. J., Müller, A. and Shail, R. K. (2010) 'Source and partitioning of B and Sn in the  
704 Cornubian batholith of southwest England', *Ore Geology Reviews*. Elsevier B.V., 38(1–2), pp. 1–8.

705 Yang, H., Zhang, H., Luo, B., Gao, Z., Guo, L., & Xu, W. (2016). Generation of peraluminous granitic  
706 magma in a post-collisional setting: a case study from the eastern Qilian orogen, NE Tibetan  
707 Plateau. *Gondwana Research*, 36, pp. 28-45.

## 708 **Figure Captions**

709 **Figure 1.** Surface expressions of the Cornubian Batholith in SW England (modified from Dangerfield &  
710 Hawkes 1981; Exley & Stone 1982; Simons et al., 2016) with an inset map of the Crownhill area  
711 (modified from Knox & Jackson, 1990). \*VP, variably porphyritic; HD, Hingston Down; KH, Kit Hill; BB,  
712 Belowda Beacon; CD, Castle-an-Dinas; CH, Cligga Head; SA, St. Agnes; CB, Carn Brea; CM, Carn Marth.

713 **Figure 2.** Compilation of the previous geochronological studies of granites and associated  
714 mineralisation within the Cornubian Batholith. G1 represents the two-mica and muscovite granites  
715 and G2 represents biotite and tourmaline granites. <sup>1</sup>Nance et al., (2010); <sup>2</sup>Shail & Alexander (1997);  
716 <sup>3</sup>Chadwick & Evans (1995); <sup>4</sup>Neace et al., (2015); <sup>5</sup>Chesley et al., (1993); <sup>6</sup>Chen et al., (1993); <sup>7</sup>Clark et  
717 al., (1993); <sup>8</sup>Darbyshire & Shepherd (1987). Fl, Fluorite; SC, South Crofty; WR, Wheal Remfry; GSV,  
718 Greisen-sheeted vein.

719 **Figure 3.** a. CIPW-normative QAP plot. b. Inclusions within perthitic orthoclase (HP02). c. Interstitial  
720 tourmaline amongst qtz and plg (HP06). d. Sub-hedral isolated tourmaline amongst muscovite  
721 aggregates (LM01). e. Twinned cassiterite crystals within tourmaline vein (HP05). f. Zircon within

722 quartz phenocryst (HP01). g. Zircon from TG, displaying zoning and a monazite inclusion (HP05). h.  
723 Zircon from BG displaying internal zoning and a metamict crust (HP02). Qtz, quartz; Bt, biotite; Or,  
724 orthoclase; Plg, plagioclase; Tur, tourmaline; Ms, muscovite; Cst, cassiterite; Zrn, zircon; Mnz,  
725 monazite; Ap, apatite.

726 **Figure 4.** Whole-rock geochemistry plots, where plots b-e are underlain with granite geochemistry  
727 collated from Simons et al. (2016). a. A/NK versus A/CNK diagram. b. MgO versus SiO<sub>2</sub>. c. Zr versus  
728 TiO<sub>2</sub>, overlain with the Zr saturation threshold (Watson & Harrison, 1983). d. Rb versus TiO<sub>2</sub>. e. Zr  
729 versus Nb with ratios overlain from Manning et al., (1996). f. Nb/Ta versus TiO<sub>2</sub> with magmatic-  
730 hydrothermal transition (MHT) index numbers. g-h. Rare earth element spider plots for BG (g) and TG  
731 (h), normalised to the chondrite values of Boynton (1985).

732 **Figure 5.** a. Back-scatter electron images of ablated zircon grains with their corresponding ages. b. LA-  
733 ICP-MS Tera-Wasserburg diagram of BG zircon cores and rims, with regression line fixed at 0.85 after  
734 Stacey & Kramers (1975) model, presented ages are weighted averages. c. LA-ICP-MS Tera-  
735 Wasserburg diagram of TG zircon cores and rims, with fixed regression line and weighted average  
736 ages. d. Concordia plot of BG and TG samples from CA-ID-TIMS analysis. e. CA-ID-TIMS calculated and  
737 weighted average ages from BG and TG.

738 **Figure 6.** LA-ICP-MS U-Pb monazite geochronology for monazite inclusions within zircon rims. Only  
739 monazite inclusions within zircon grains from BGs were capable of being dated, due to their size and  
740 homogeneity. The age presented is a mean concordia age of <sup>206</sup>Pb/<sup>238</sup>U (2σ).

741 **Figure 7.** a-d Th/U against Hf, Sc, Nb/Ta and Gd/Yb. e-f. Chondrite-normalised REE plots (Boynton,  
742 1985), where both granite types display similar trends, with variably positive Ce anomalies and  
743 pronounced negative Eu anomalies.

744 **Figure 8.** a. The internal morphology of zircon grains used for this study. Monazite inclusions are  
745 exclusive to zircon rims. b.  $^{238}\text{U}/^{206}\text{Pb}$  ages (Ma) against Th/U of all geochronological analyses from this  
746 study.

#### 747 **Table Captions**

748 **Table 1.** Petrographic summary of the granite types sampled for this study.

749

#### 750 **Supplementary Data**

751 **Supplementary Figure 1.** a. LA-ICP-MS Tera-Wasserburg diagram of BG zircon cores and rims from  
752 Blackenstone Quarry, with regression line fixed at 0.85 after Stacey & Kramers (1975) model,  
753 presented ages are weighted averages. b. LA-ICP-MS Tera-Wasserburg diagram of BG zircon cores  
754 and rims from Lee Moor. c. Results from concordant analysis obtained from CA-ID-TIMS analysis of  
755 Blackenstone BG zircon grains. Here it is presented with calculated and weighted average ages. d.  
756 Results from concordant analysis obtained from CA-ID-TIMS analysis of Lee Moor TG.

757 **Supplementary Table 1.** Whole-rock geochemistry for samples used for this study.

758 **Supplementary Table 2.** LA-ICP-MS U-Pb zircon geochronology dataset for granites at Crownhill.

759 **Supplementary Table 3.** LA-ICP-MS U-Pb monazite geochronology dataset for BG at Crownhill.

760 **Supplementary Table 4.** CA-ID-TIMS U-Pb zircon geochronology dataset for granites at Crownhill.

761 **Supplementary Table 5.** Representative dataset for LA-ICP-MS zircon trace element analysis, including  
762 the Ti-in-Zrn thermometer [1] (Watson & Harrison, 1983).

763

764

765



**Table 1.** Petrographic summary of the granite types sampled for this study.

Granite	Biotite Granite (BG)	Tourmaline Granite (TG)
Grain Size	Predominately medium to coarse grained, up to megacrystic	Fine to medium grained
Texture	Moderately to strongly porphyritic with Or (6-15 mm) and Qtz (2-10 mm) phenocrysts	Weakly porphyritic with Or (ca. 5 mm) and Qtz (1-3 mm) phenocrysts
Grain Dispersal	All minerals dispersed throughout samples	Clusters of interstitial tourmaline and poorly distributed aggregates of muscovite
Major Mineralogy	Qtz, Or, Pl, Bt	Qtz, Or, Pl, Tur, Ms
Minor Mineralogy	Ms, Tur, Zrn, Ap, Mnz, Xtm, Fe-oxide	Bt, Zrn, Ap, Mnz, Xtm, Cst, Fe-oxide
Notes	Two-stage Or phenocryst growth. Minor argillic alteration of Pl.	Aggregates of Ms. Interstitial Tur replacing Bt. Greater degree of argillic alteration of Pl and Or.

766

767

768

769

770

771

772

773

774

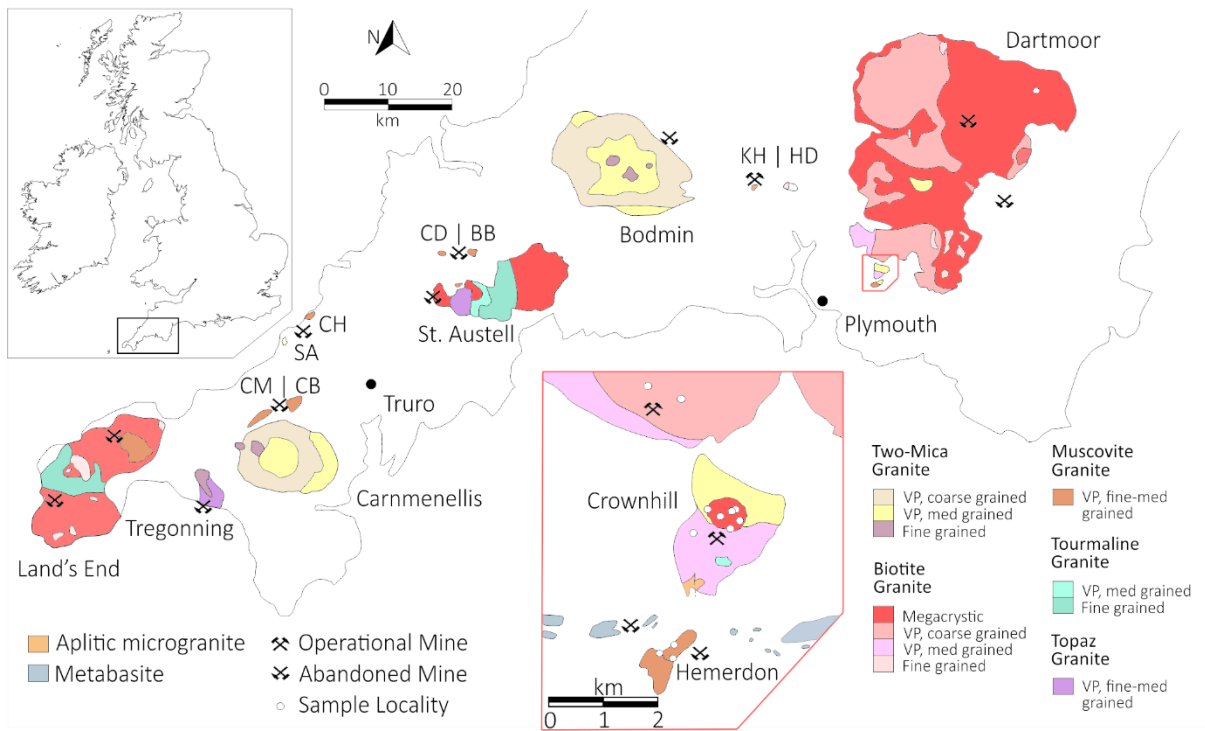
775

776

777

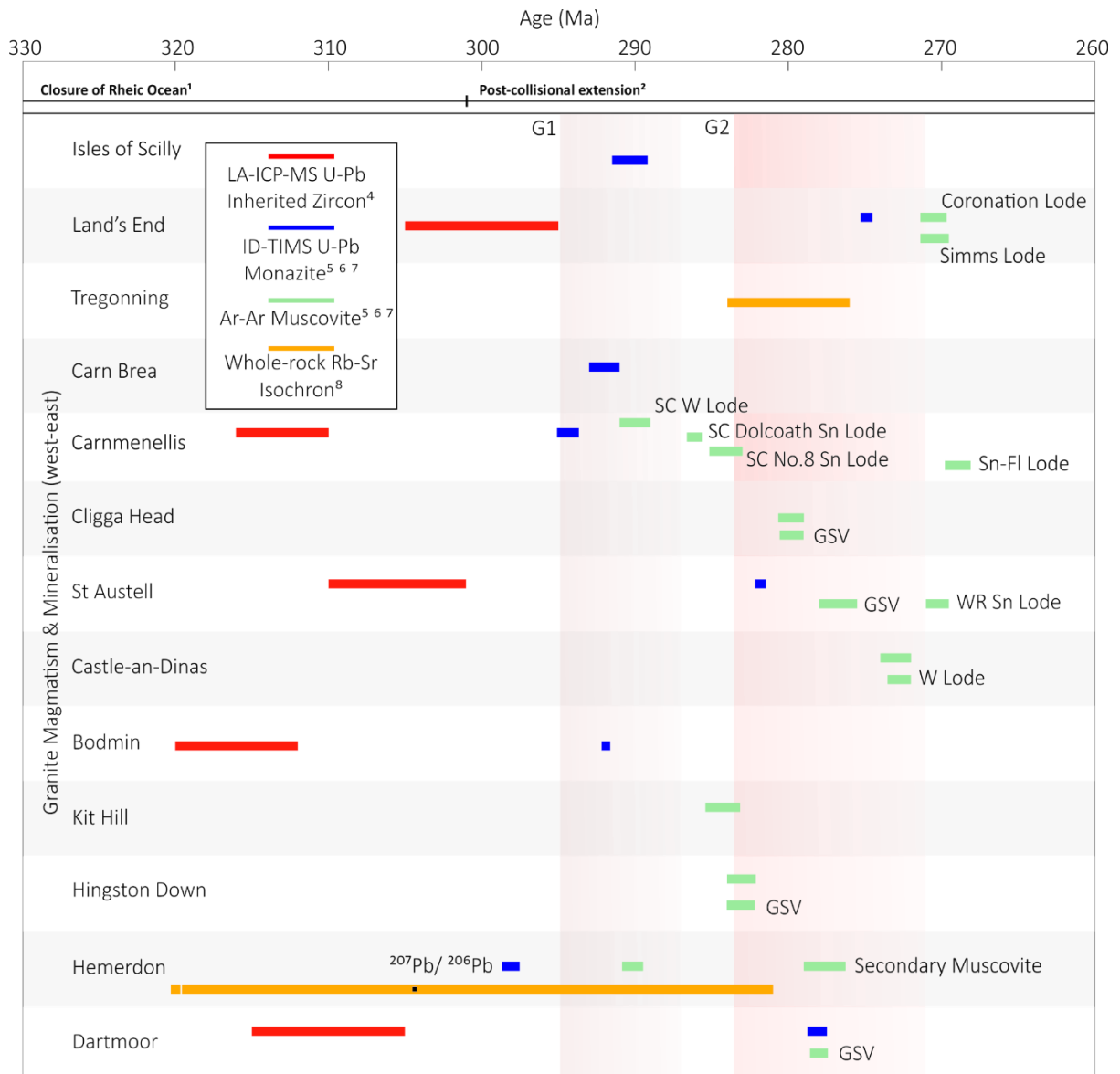
778

779 Figure 1

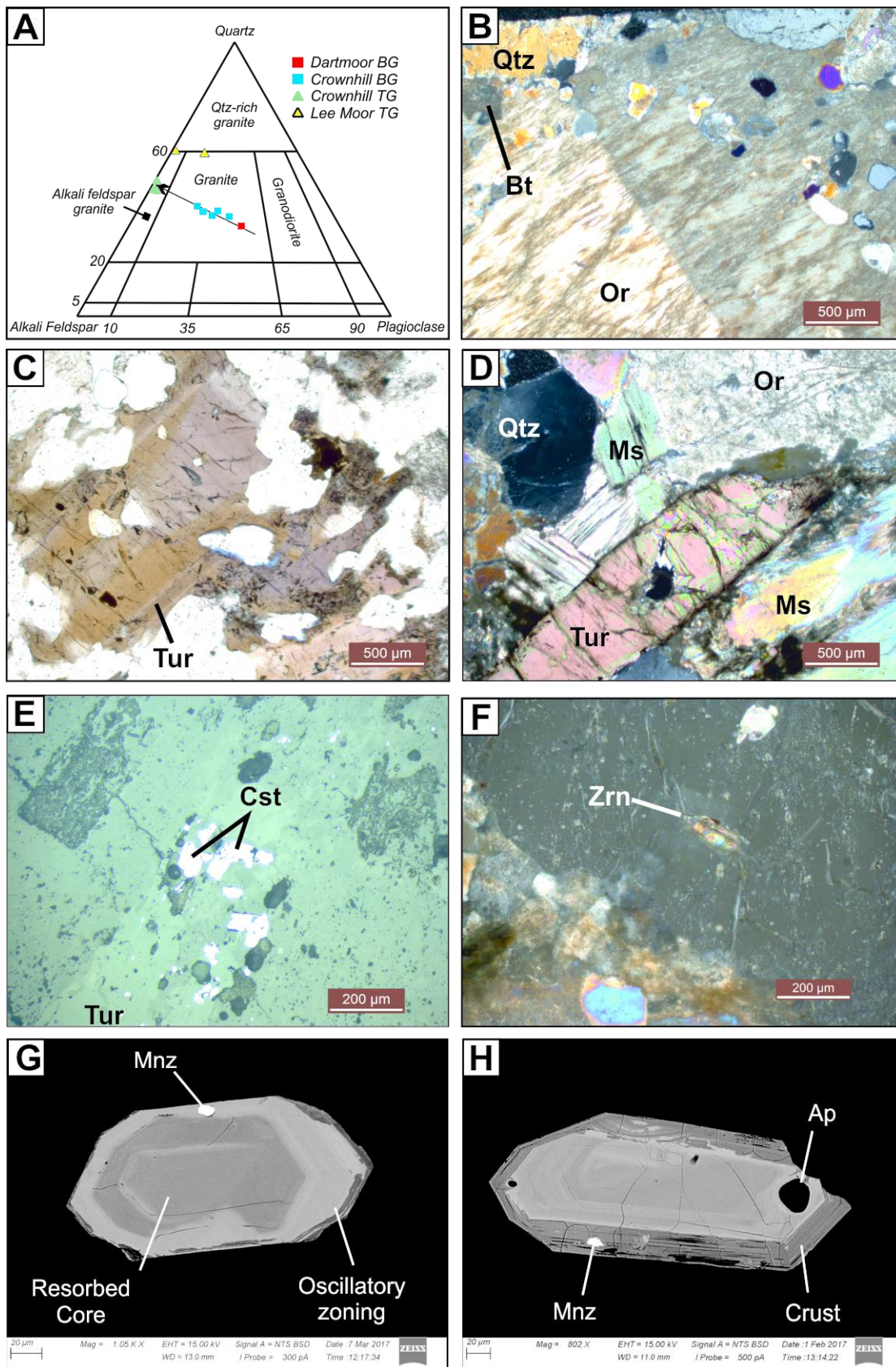


780

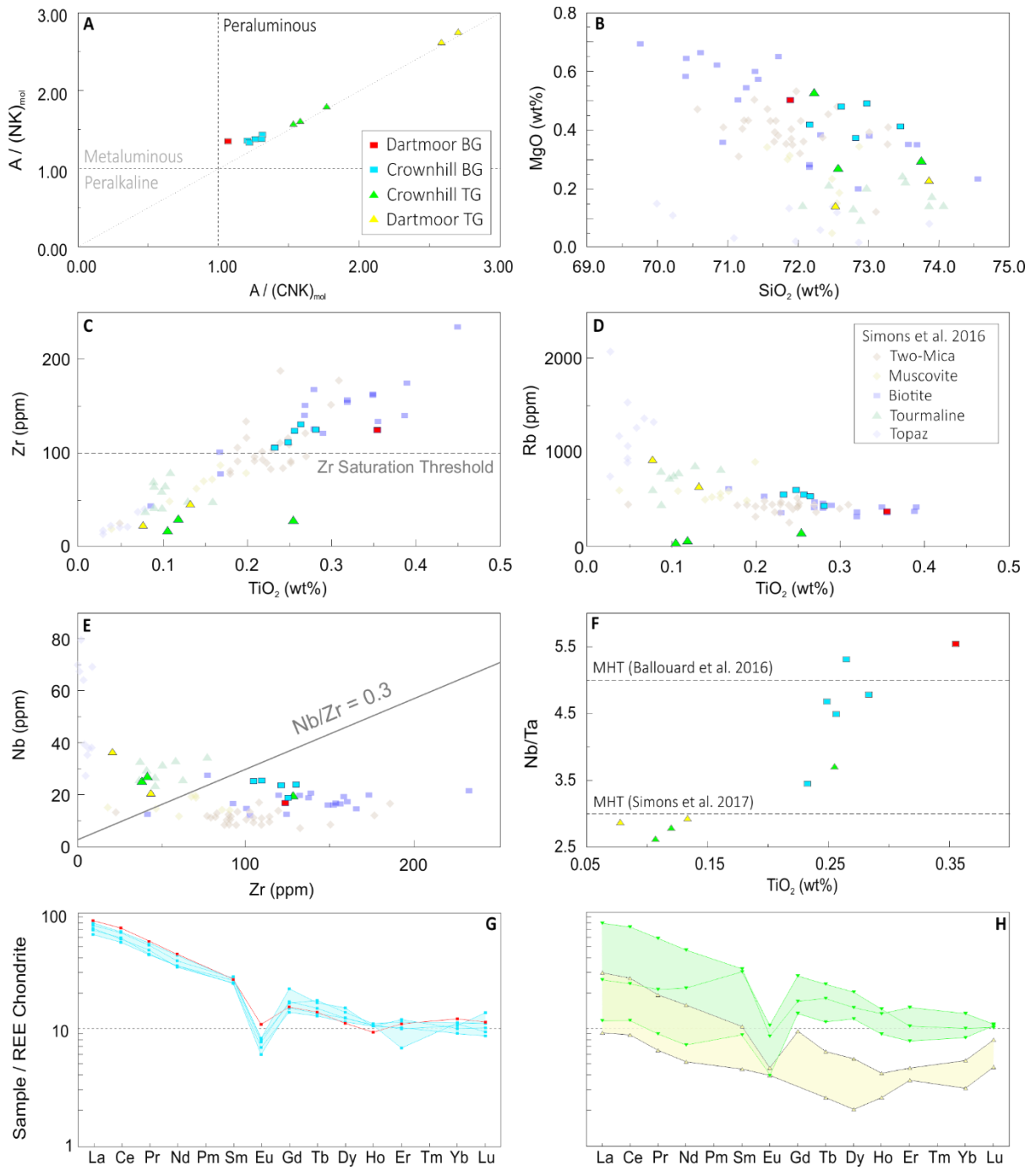
781 Figure 2



782



785 **Figure 4**

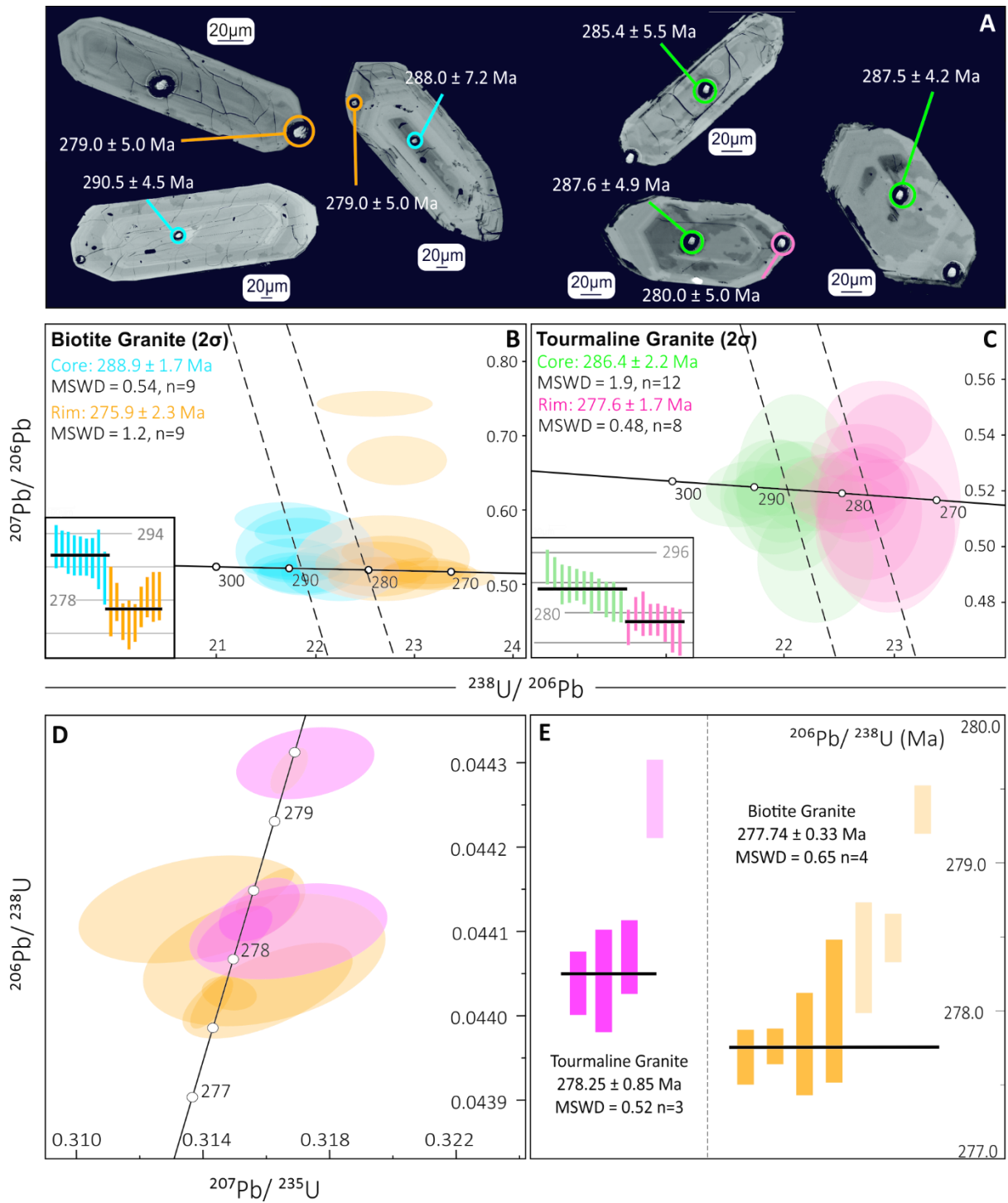


786

787

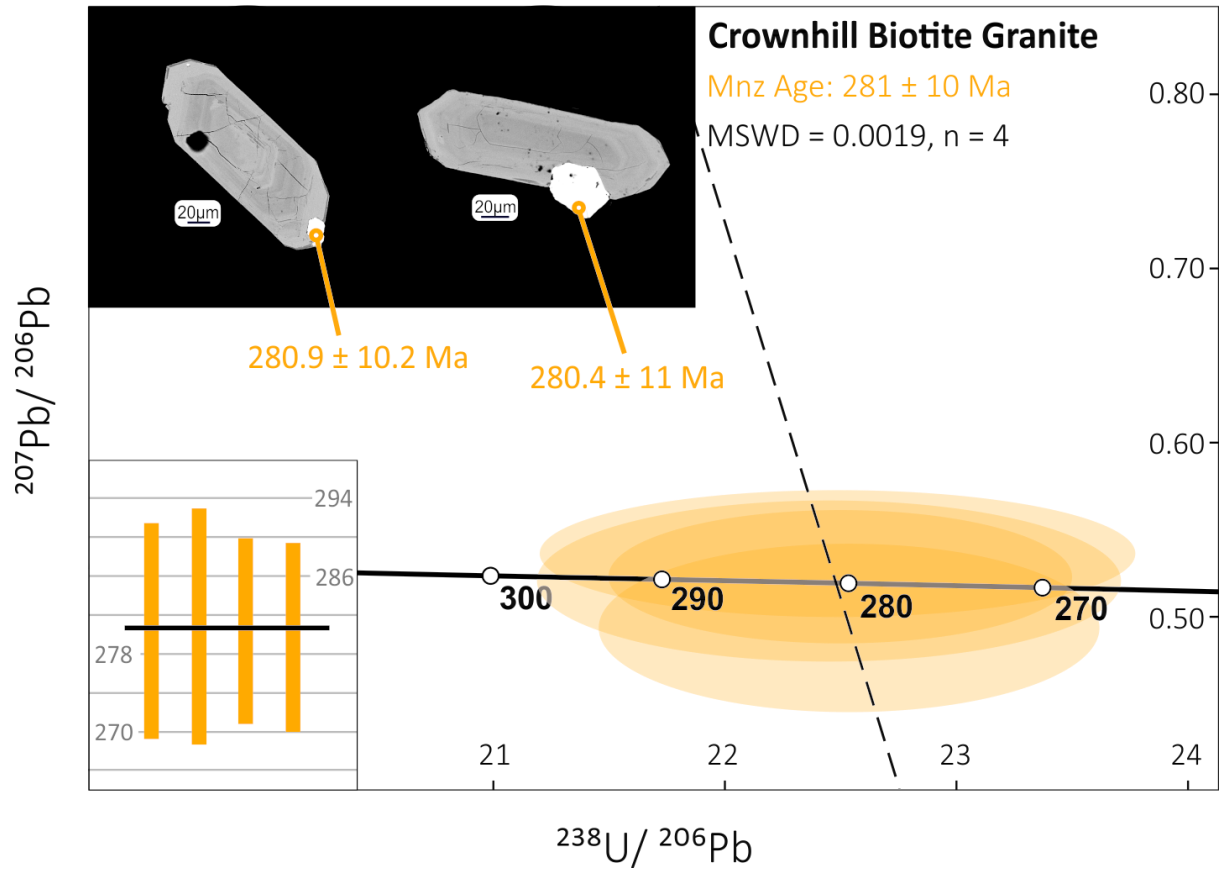
788 Figure 5

789



790

791 Figure 6

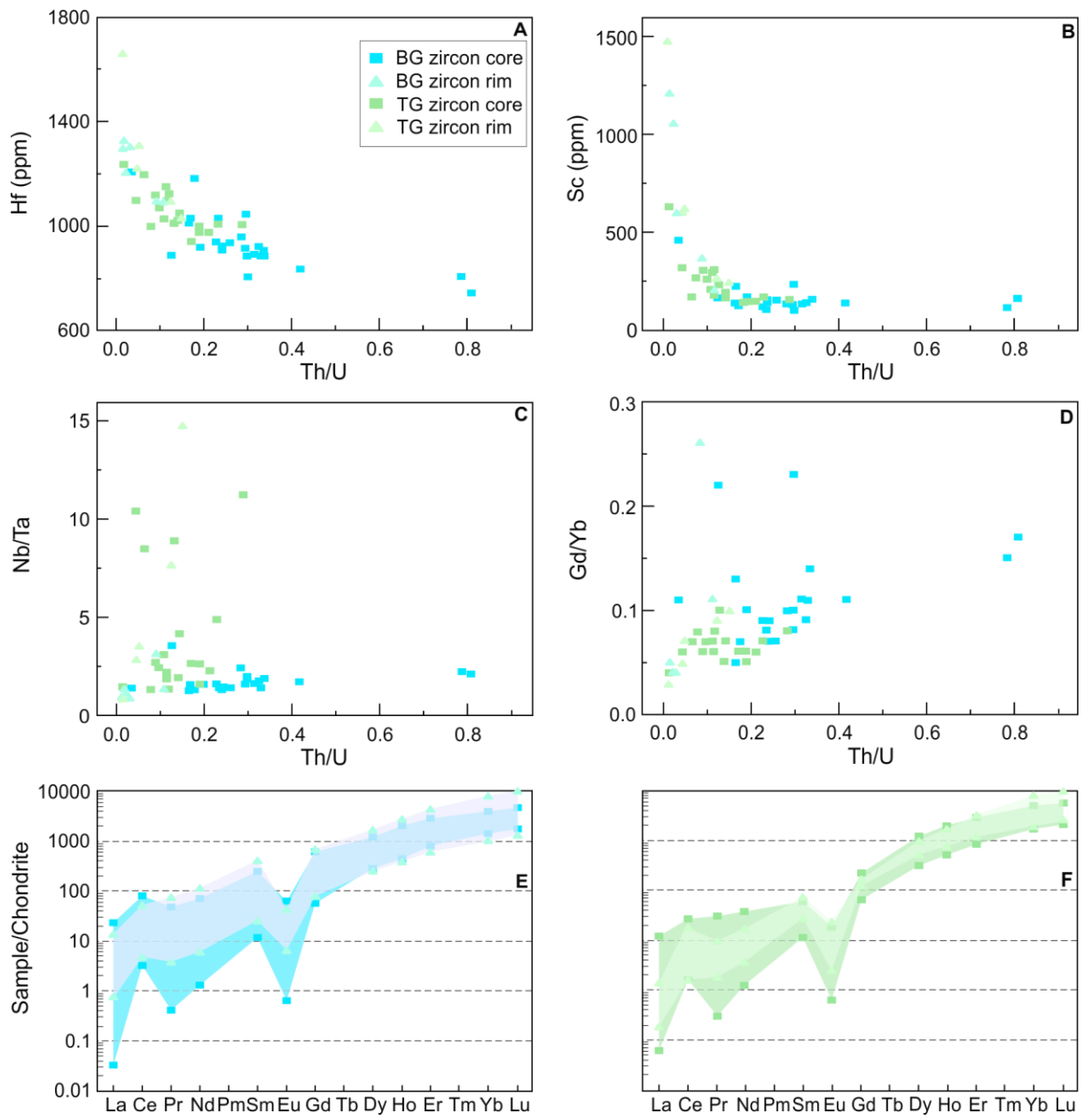


792

793

794 Figure 7

795

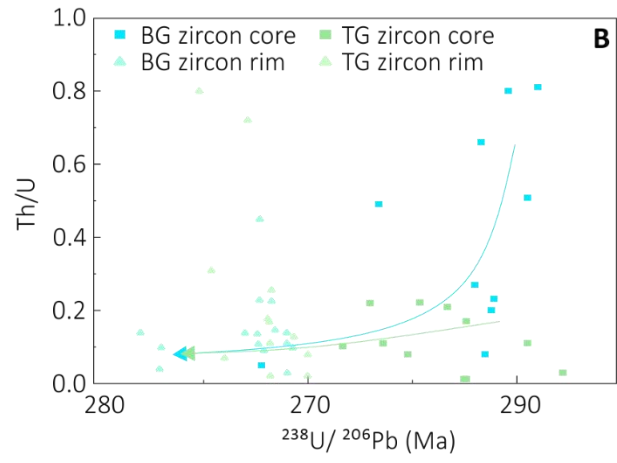
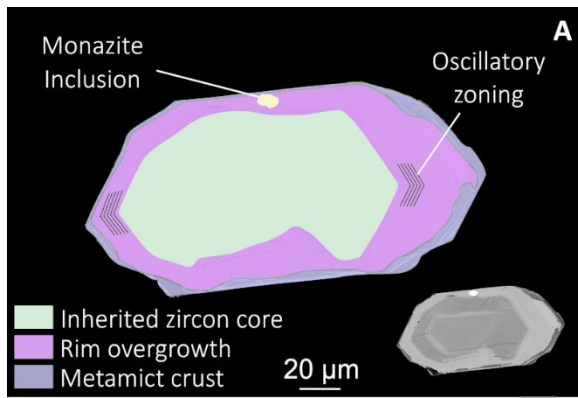


796



797 Figure 8

798



799